Determination of Bulk Dimensional Variation in Castings
FINAL REPORT

Project Title: Determination of Bulk Dimensional Variation in Castings

Date of Report: April 14, 2005

Recipient: University of North Carolina at Charlotte
9201 University City Blvd.
Charlotte, NC 28223-0001

Period of Performance:

Award Number: DE-FC36-02ID14231

Subcontractors: Dr. Thomas Piwonka
The University of Alabama
Box 870201, 106 Bevill Building
Tuscaloosa, AL 35487-0201
Phone: 205-348-1589
E-mail: tpiwonka@coe.eng.ua.edu
Congressional District 7

Contact(s): Dr. James F. Cuttino, Associate Professor
The Department of Mechanical Engineering and Engineering Science
The University of North Carolina at Charlotte
9201 University City Boulevard
Charlotte, NC 28223
Phone: 704-687-3335
E-mail: jcuttino@uncc.edu
Congressional District 12

Project Team: DOE-HQ contact – Ehr-Ping Huangfu; DOE Technical Monitor, Chico Gonzalez; Project Manager - Dr. Dibyajyoti Aichbhaumik; Contract Specialist –Stephanie Carabajal; Industry Contact – John Andrews (steering committee)

Acknowledgment: This report is based upon work supported by the U. S. Department of Energy under Award No. DE-FC36-02ID14231.

TABLE OF CONTENTS

List of Figures

List of Tables

Project Overview

The purpose of this work is to improve the efficiency of green sand foundries so that they may continue to compete as the most cost-effective method of fabrication while meeting tightening constraints on near-net shape manufacturing. In order to achieve this objective, the study is divided into two major components. The first component concentrated on identifying which processes control surface finish on the castings and which provide potential reductions in variations. The second component identified metrological methods that effectively discern between the geometry of bulk material versus surface finish in order to more accurately determine the quality of a part.

The research resulted in the determination of an empirical relationship relating pouring parameters to dimensional variation, with an R^2 value of greater than 0.79. A significant difference in variations obtained from vertical vs. horizontal molding machines was also noticed. When analyzed separately, however, the resulting empirical relationships for horizontal and vertical machines had reduced R^2 values, probably due to the reduced data sets. Significant parameters when considering vertical and horizontal molding machines together included surface roughness, pattern type, iron type, pouring rate, copper content, amount of Western Bentonite, and permeability.

When considering horizontal molding machines separately, surface roughness, pouring rate, Manganese, Sulfer, and Copper content in the melt, amount of Western Bentonite, and mold permeability had significant impact on the regressions (Note however that the percent copper seems to influence standard deviation positively in the horizontal regression and does the opposite in the full model). Vertically parted machines had a higher sensitivity to pouring rate, Silicon, Manganese and Phosophorus content in the melt.

The horizontally parting pattern yield standard deviation values that are more dependent on placement in the mold, i.e. the thinner webs placed closer to the feed sprue have less variation than when they are oriented near the outer edge of the mold. Contrasting that, the thicker webs placed closer to the edge of the mold tend to have less variation than those placed closer to the gating.

A metrology round robin was conducted to determine the effectiveness of common metrology practices in the industry. The results were startling, showing excessive differences from one foundry to another in reporting dimensions. Results from this portion of the study were so severe that they could only indicate a strong need for metrology training and standardization in the industry.

Finally, it was determined that the surface waviness had more impact on dimensional variation than does surface roughness. The exception to this rule is when burn-in occurs, which is very detrimental to dimensional repeatability. Burn-in occurred much more frequently in the horizontal castings, partly because of the lower clay content, higher temperatures, and lower compactability.

Introduction

Iron castings have a long history of use in automotive and other industries due to high availability and low cost. In an effort to improve fuel economy and to reduce emissions in automobiles, the reduction of gross vehicle weight has been an objective of most manufacturers. To meet this objective, automobile manufacturers have sought to use alternative lighter-weight metals such as aluminum in the production of engine blocks, cylinder heads, and frame and suspension components. The iron casting industry has responded by encouraging foundries and researchers to investigate the production of thin wall iron castings in order to reduce the weight of the castings so that they can be competitive with aluminum components. Several approaches have been adopted in an attempt to produce thin wall iron castings; these are reviewed and explained by Kachru in his thesis [1]. However, few techniques address the issue of producing thin wall iron castings using green sand molding. In his thesis, Kachru reports on the molding capability of thin wall iron castings using green sand.

Green sand molding is the most cost-effective method for producing castings. However, its centuries-old heritage has led to the belief that green sand molding is an “old” art, and that new, advanced casting processes are required to fabricate near-net shape products. In addition, the minimum tolerances for green sand molding are often reported to be as high as $\pm$1 mm for even the smallest features, resulting in “thin” features that are oversized in anticipation of manufacturing fluctuations. In the past, wall thicknesses and parting line alignments could vary by several millimeters without influencing the function of the part. This sort of variability would clearly be disastrous for parts with sections only 3mm thick.

The implications of large dimensional variations are significant in terms of energy and raw materials. The practice of routinely oversizing casting features to allow for large manufacturing variations results in energy costs resulting from melting more material and increased weight in final products. Excessive variations also result in high scrap rates, increased casting defects (such as flash and shift), and increased cleanup efforts such as grinding. Alternative methods to green sand molds have been developed in attempts to overcome the variability issues, but those efforts often require complex steps and costly equipment development. This project addresses these issues by optimizing the green sand molding process to provide more accurate products with tighter tolerances. If dimensional variations can be reduced, products will be designed that come nearer to net-shape, reducing the need to “over-design” and the need for extensive finishing.

Along with the challenges of producing such castings come difficulties in measuring the castings accurately. The cultural change necessary within foundry layout (i.e. inspection) facilities to specify and verify these tighter requirements is not trivial. The scope of this research was limited to the technical aspects of measuring thin-walled components with CMMs. There are a number of factors which influence the results of using coordinate metrology on castings. In this paper we focus on geometrical characteristics that introduce uncertainty in assessing the "true" value for the profile or thickness of cast components. One of the major factors affecting the dimensional variation in iron castings is the magnitude of surface characteristics such as roughness and waviness, as the casting surface can be very uneven due to the sand penetration defects found in some castings. Several studies have shown that shot peening process improve Casting surface quality [2] and also reduce dimensional variation. Instead of shot peening, sand blasting was used as the finishing process to clean up the castings used in this study, as the thin sections with 3 mm thickness were warped when they were shot peened. Prediction and optimization of form error measurement for industrial surfaces was studied by Mestre and Abou-Kandil [3] using statistical methods. No articles have been found that dealt specifically with the surface wavelength composition of green sand iron castings and its effects on CMM measurements. A procedure is presented for reducing the uncertainty in the thickness measurements obtained from CMM by comparing the measurements obtained from profilometry with CMM measurements by filtering the surface data using standard Gaussian filter [4] and Morphological filter [5-7].

Research Procedure

The project incorporates two round-robin studies based on castings produced in participating foundries and measured in various metrology shops. The castings are produced using a common pattern developed during Phase I of the study. The vertically parting pattern is shown in Figure 1, and a representative casting is shown in Figure 2.

Figure 1: 2-on Vertically Parting Pattern

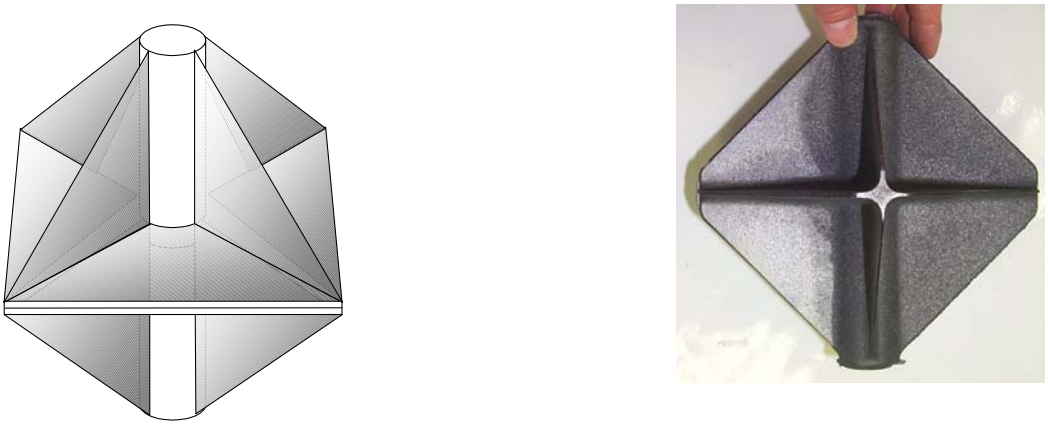

Figure 2: Sample casting

The new pattern was designed to fit on the smallest of the DISA machines, the 2013, so that it could be run on virtually any DISA vertically parting machine using a bolster if necessary. The fin thicknesses are extremely small, ranging from 1.3 mm – 6 mm. The reduced thicknesses were designed to provide experimental identification of the threshold for the fabrication of sound thin-walled castings. The gating was designed to come up through the center of the casting in a 1.25" cylinder to provide optimal filling.

The layout of the two serials is non-symmetric, with serial 1 having its thinnest fins adjacent to the down sprue and serial 2 having its away from the sprue, near the exterior surface of the mold. This allows examination of the effects of heat transfer rates on the quality of the castings, since the thinnest fin of serial 1 is located next to the down sprue (presumably slowing cooling rates) while the thinnest fin of serial 2 is located near the exterior mold wall.

During the course of this project, several foundries expressed interest in participating in the study with a horizontally parted pattern. Design of the horizontal pattern was conducted with the assistance of Dan Westphal of Brillion Iron Works. The pattern is shown in Figure 3. The drawings have been shipped to MagmaSoft corporation for simulation of the pouring process. This simulation was used in the design of the vertical pattern

that was used in Phase I of the study and was instrumental in identifying weaknesses in the design. We will be using the simulation again here to identify potential flaws that may occur due to poor gating or pattern design.

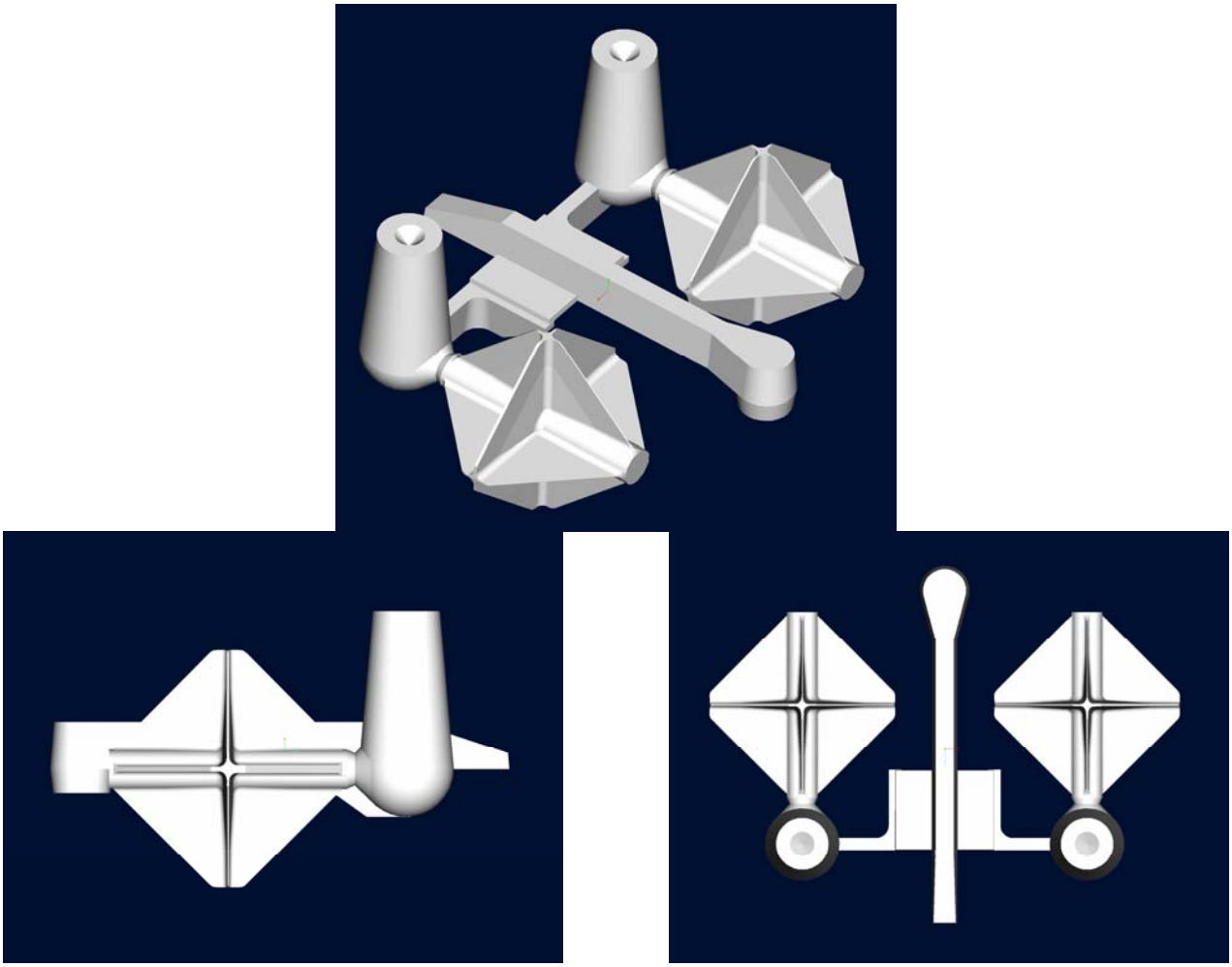

Figure 3: Different Views of Horizontal Pattern

Bulk Metrology of Castings

All measurements were conducted in a temperature controlled environment maintained at $20.0^{\pm}0.1^{o}$C. The parts were located centrally on the coordinate axes of the CMM. A kinematic fixture as shown in Figure 4 was used to restrain the casting in six degrees of freedom on the CMM. The fixture consisted of three precision balls mounted on pillars, each ball contacting the casting on two orthogonal sides to constrain motion in all degrees of freedom. All measurements were completed with the part in the fixtured position shown.

In this study, it is assumed that most of the variation measured is a result of the variation inherent within the parts. This is assumed because there are no apparent problems with repeatable fixturing of the parts and the known repeatability of the coordinate measuring machine used is well below the variation reported for the parts. A gage R&R study was conducted to verify this assumption and to give a statistical analysis of the variation in the measurement methodology.

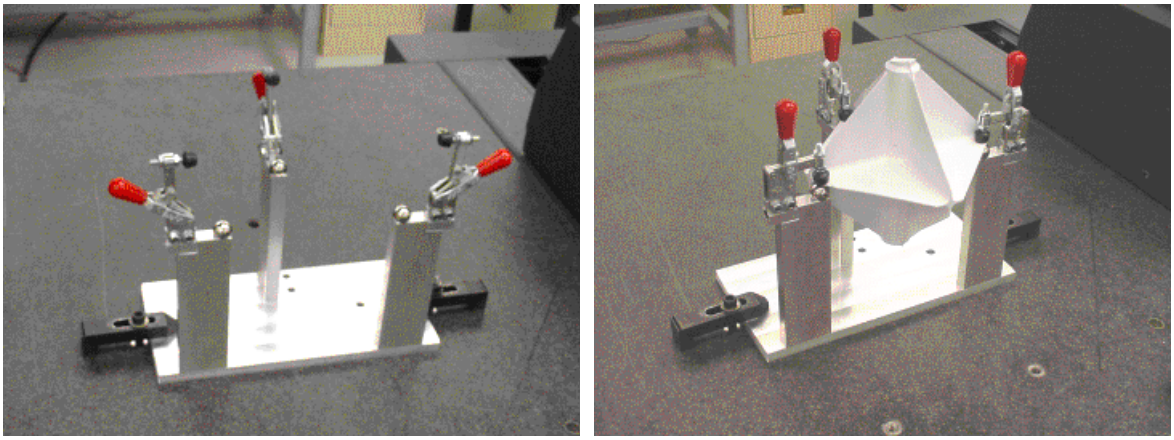

Figure 4: Locating Fixture

A Brown and Sharpe XCel 765 Coordinate Measuring Machine (CMM) was used to measure the castings, and a CNC program was written to conduct the measurements using QUINDOS software. The measuring program establishes a metrology coordinate system by sampling a subset of the fins on the casting. The planes of the coordinate system nominally pass through the middle of the fins (e.g., the *x-y plane* passes through the middle of the four horizontal fins). Each fin is then sampled with either ten or eleven points per fin surface depending on the location of the fins. Measurement points are collected from each side of the fin, and a midpoint and thickness is calculated for each location. The sampling patterns are shown in Figure 5. The modified pattern shown in Figure 5(b) allows for the fixture while still maintaining alignment of the points for future analysis of warp in the castings.

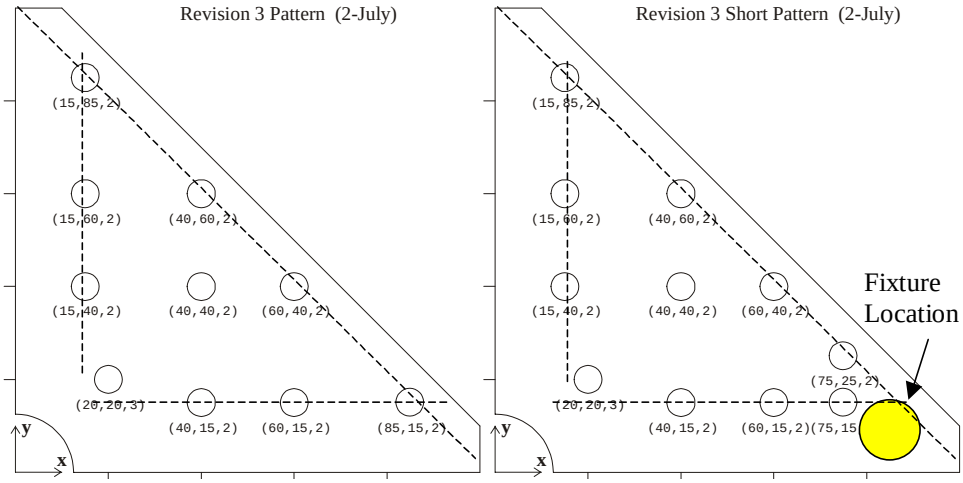

Figure 5: Sampling Patterns

Finishing Processes

The cleaning and finishing processes for different test cases have been closely monitored to observe possible affects on standard deviation of thickness values for the test specimens. Early in the study certain observations were made concerning shot and sand blasting finishing processes. In general, past data has shown that "peening" or shot blasting finishing processes have affected measured standard deviation values by reducing deviation values exponentially with increased exposure time. Sand blasting processes have typically had less of an impact on the standard deviation values.

The effects of these finishing processes on standard deviation values can be seen in the figures below from a earlier measured test case. Figure 6 and Figure 7 show the standard deviations of point thickness values vs. measured point thickness values for Serial 1 of test case "X". Serial 2 is not shown here. (Recall that in this parametric study there are 2 serials per test case, each having different orientations on the test pattern).

Figure 8 and Figure 9 show histograms of the Serial 1 standard deviation data in Figure 6 and Figure 7 with similar data from Serial 2. By comparing the shot and sand blasted results, one can see that standard deviation values are lower in most point thickness ranges for the shot blasted case.

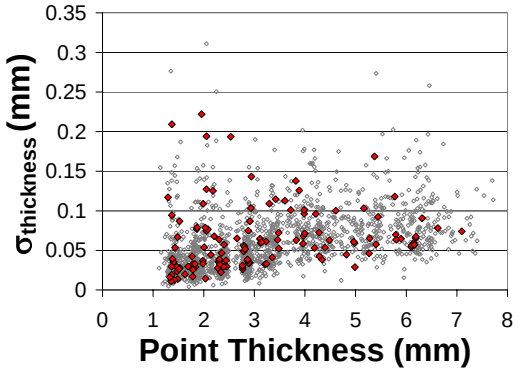

Figure 6 – "X" Test Case Serial 1 (Sand Blasted) Results

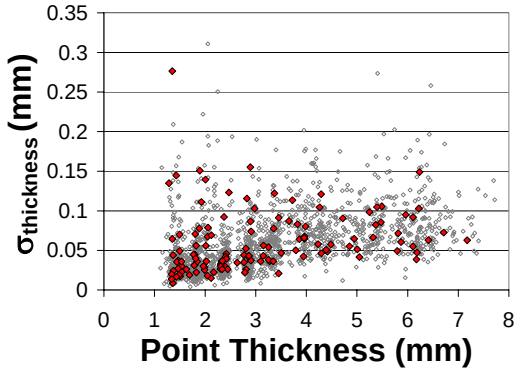

Figure 7 – "X" Test Case Serial 1 (Shot Blasted) Results

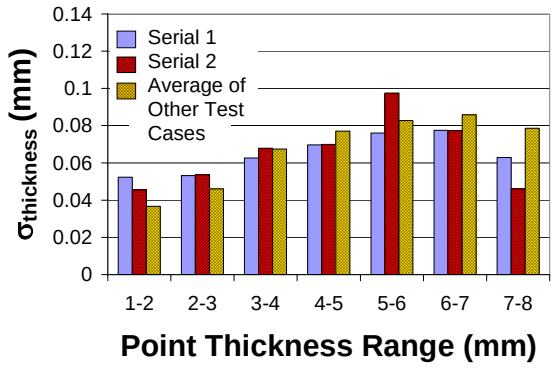

Figure 8 – Histogram of Point Thickness for "X" Test Case, (Shot Blasted) Results

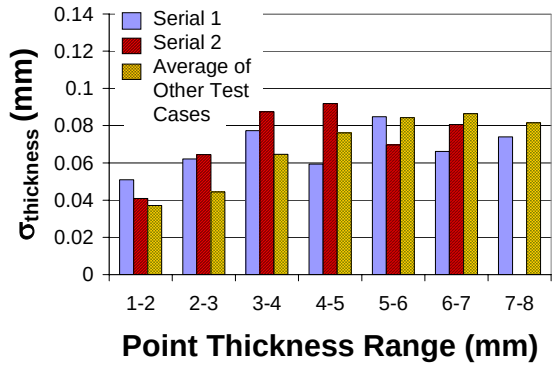

Figure 9: Histogram of Point Thickness for "X" Test Case, (Sand Blasted) Results

After observing these results, and considering past indications of shot blasting effects on standard deviation values, it was concluded that future studies should include principally sand blasted finishing processes. The intention was to isolate the production process parameters from the finishing effects. Sand blasting would have less impact on measurements while providing the necessary cleaning for the test specimens prior to the CMM measuring process.

Defects Observed with Horizontal Pattern

When the horizontal pattern was created and test runs using the horizontal pattern had been made at several foundries, it was observerd that castings produced with this pattern had some defects that may be associated with the design of the pattern. Figure 10 shows examples of some of the defects that have been observed.

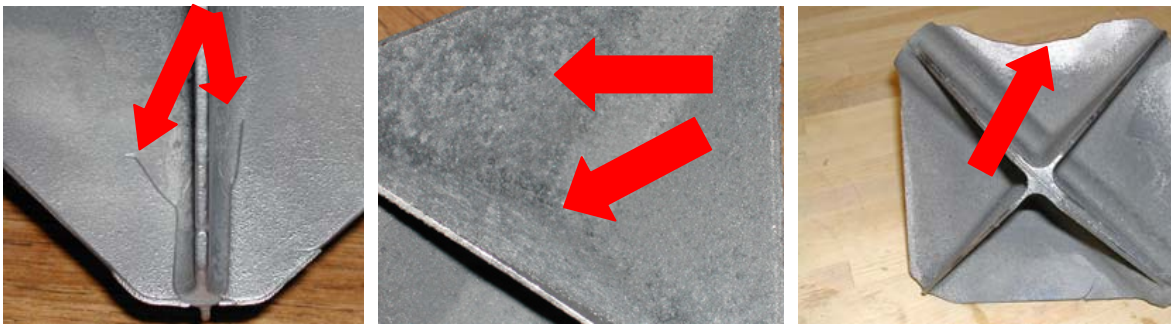

A: Cold Shut **B: Burn-in** **C: Misrun**

Figure 10: Defects Using Horizontal Pattern

In Figure 10A the web has a distinct separation of material. The defect, which has also been observed in castings made with the vertical pattern, are much larger and more numerous when the horizontal pattern is used. The defect occurs on the thinnest webs and seems to be a result of cold shut that is likely caused by high metal velocities (due to the constricted area), and multiple flow fronts. Figure 10B shows severe burn-in experienced in many of the castings. The burn-in is more severe in some pours than others, and is often prevalent enough that measurements in roughness are foregone to prevent damage to the profilometer instrumentation. The burn-in also affects measurements for bulk dimensional analysis since it adds a considerable amount of nonstructural material. Figure 10C shows a misrun defect which is common to almost every part produced in the initial runs with the horizontal pattern. The defect almost exclusively occurs on the thinnest web in the cope.

Pouring Simulations

Magmasoft committed to donate simulated pouring data for this study. Several scenarios were proposed by UNCC pertaining to defects which have occurred in many of the test cases. Each case proposed includes a description of the specific defect and recorded parameters used in producing the part (note: the lists are abbreviated in this report).

Case A: Burn-in

Large areas of “burn-in” such as that shown in Figure 11 have been observed in most samples produced with the horizontal pattern. However, some casting defects do not appear to be as severe as others. In particular, one test case poured with the horizontal pattern has very little burn-in. There are two parameter sets that would be good candidates for simulation. They are labeled “Case A: 1” and “Case A: 2”. A:1 is the test case with very little burn-in, and A:2 is a test case that had a large percentage of surface area affected by the defect.
Table 1 is a partial list of parameters recorded and includes the parameters with the most notable variations between test cases.

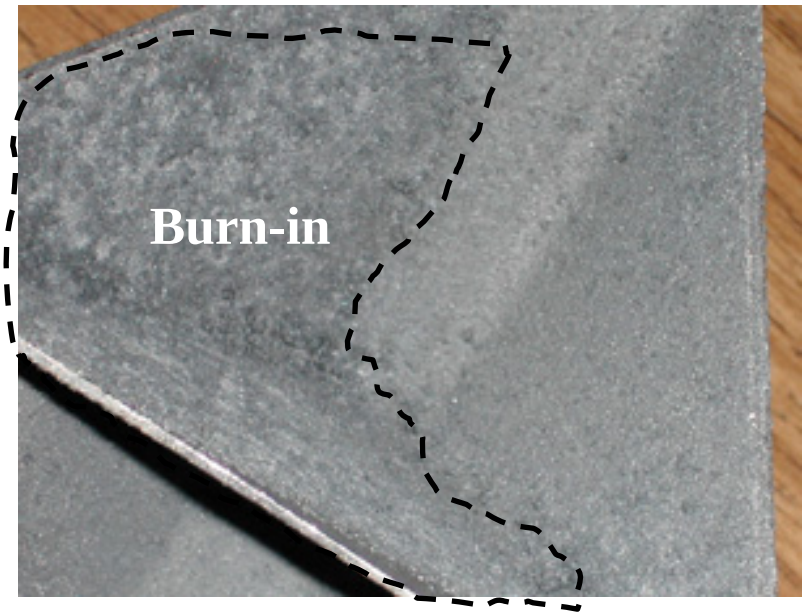

Figure 11: Case A, Burn-in Defect

Table 1: Most Notable Parameter Variations, Case A

Case A:	Iron type	Pour. Temp	%Mg	%Green Comp. Strength	%M.B. Clay	Permeability
1 (low burn-in)	Ductile	1404	0.022	28.4	8.7	124
2 (high burn-in)	Gray	1447	0.009	25.1	9.0	132

Case B: Cold Shut

A second common defect is cold shut, which has been observed in most castings produced with the horizontal pattern, particularly where the fins intersect at the outer edge of the parts, as shown in Figure 12. For one particular test foundry where several runs of both ductile and gray iron were poured, the cold shut seemed more apparent in the ductile iron cases and less so in the gray iron castings. Table 2 shows the most notable parameter variations between the two sample test cases (note: same as in Case A).

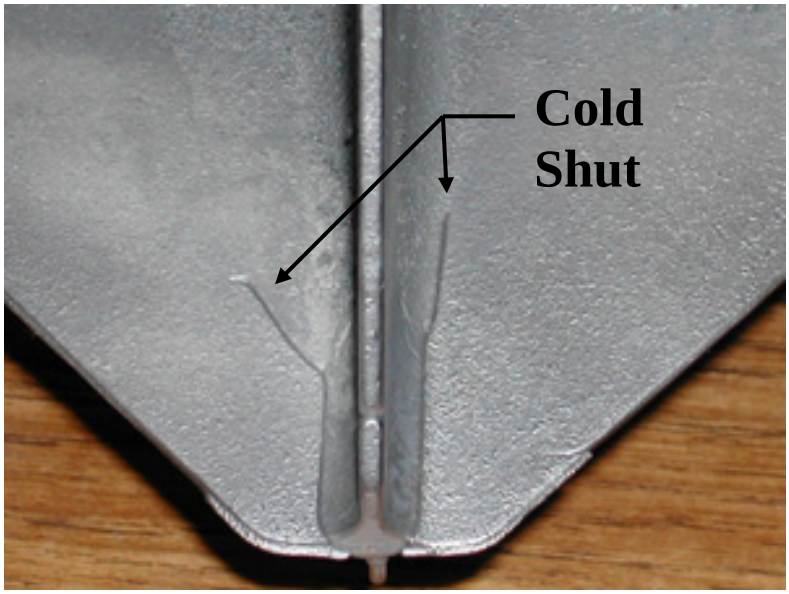

Figure 12: Case B, Cold Shut Defect

Table 2: Most Notable Parameter Variations, Case B

Case B:	Iron type	Pour. Temp	%Mg	%Green Comp. Strength	%M.B. Clay	Permeability
1 (High Cold Shut)	Ductile	1404	0.022	28.4	8.7	124
2 (Low Cold Shut)	Gray	1447	0.009	25.1	9.0	132

Case C: Misrun

Misruns like those shown in Figure 13 are common to one particular fin for castings produced with the horizontal pattern. The fin is located in the cope and is opposite to the gating where material is fed into the mold cavity. One test case has been identified as having a “low” occurrence of the misrun (Case C: 1), and one has a high occurrence of the misrun (Case C: 2). Table 3 is a partial list of parameters recorded and shows some of the major parameter variations between the two test cases.

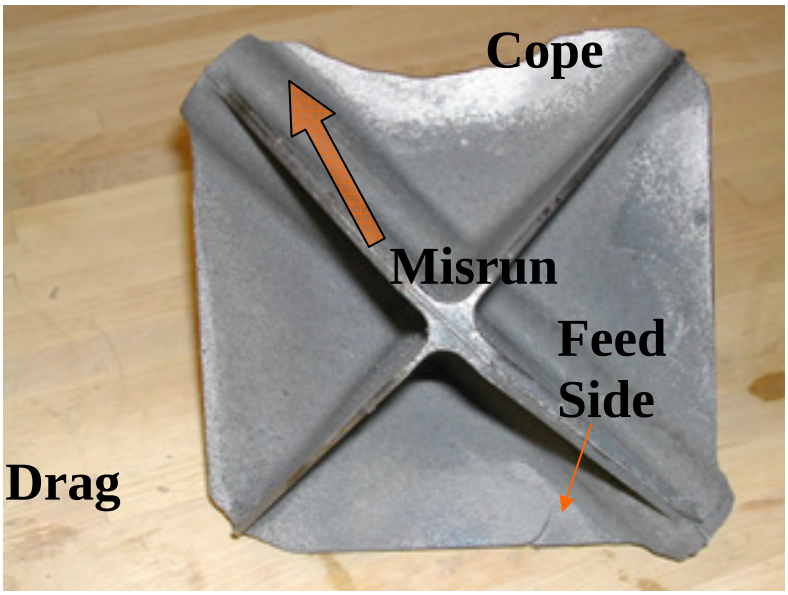

Figure 13: Case C, Misrun Defect

Table 3: Most Notable Parameter Variations, Case C

Case C:	Iron type	%Mg	%Green Comp. Strength	Permeability
1	Ductile	0.022	28.4	124
2	Ductile	0.03	25.4	116

Case D: High vs. Low % Copper Content

The percentage of copper in the casting composition is being investigated as a possible parameter that has been correlated with decreased variation in part dimension. Two test cases, "Case D:1" (low Cu@ 0.42% Cast Composition) and "Case D:2" (high Cu@ 0.64% Cast Composition) were chosen since all parameters for the two runs were very similar with the exception of the percentage of copper content in the casting composition. Both were ductile iron.

Case E: Improved Horizontal Pattern

Several defects have been observed when pouring castings using the horizontal pattern, including severe burn-in and several misrun defects. Some foundries participating in this study have given suggestions for improving the pattern design. The general consensus is that flow could be improved by venting the mold cavity in any manner of ways and some have also suggested adding a "reservoir" opposite the feed-side of the mold cavity to give the oxidized wave front entering the mold cavity a place to go outside of the part cavity. This would resemble the vertical pattern design, although the venting scheme would likely be different. For this case, a list of parameter set(s) was sent to magma for simulation and analysis of the horizontal pattern.

Magma Simulation Results:

The Magmasoft simulations were analyzed based on temperature fields in the part and the mold wall, which indicated critical values where certain defects are likely to occur. At the time of this study, variations due to copper content were not simulated.

When the horizontal castings had been completed, efforts began to optimize the pattern for better comparison with the Disa castings. To do this, we enlisted the help of Christof Heisser at Magmasoft. The most recent simulations and comments from Magmasoft have helped significantly in understanding the casting issues and are discussed in this section. Magmasoft agreed to look at Temperature field distributions for the current pattern geometry as well as for possible alternative designs. There are five configurations shown in addition to the original. Each is accompanied by the temperature field state at 100 percent fill, which would indicate where certain defects might occur. Also the current or original pattern configuration section includes an analysis of sand temperatures at the liquid metal interface when sand temperatures reach a maximum as well as a simulation of the possible effects of venting on fluid flow.

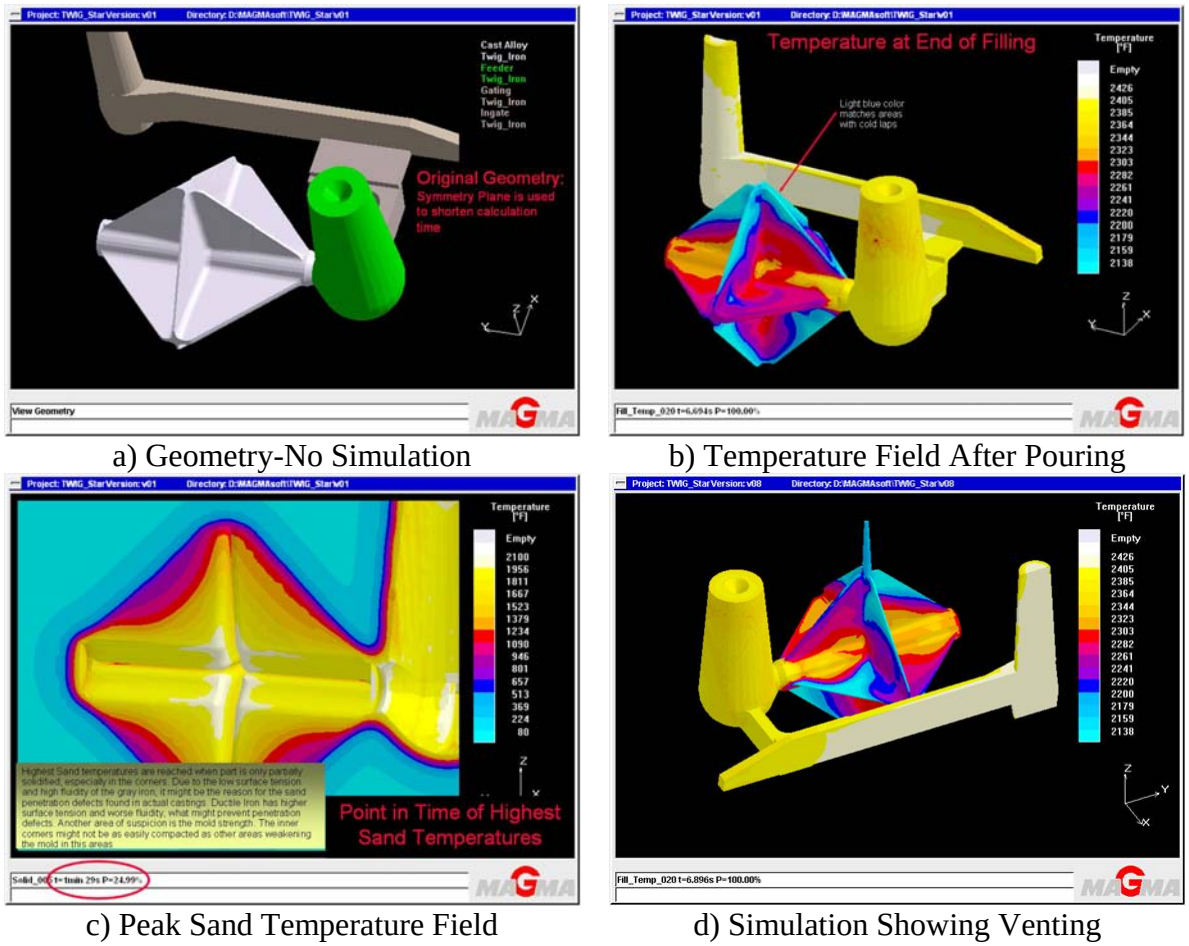

a) Geometry-No Simulation

b) Temperature Field After Pouring

c) Peak Sand Temperature Field

d) Simulation Showing Venting

Figure 14: Current Pattern Geometry

Figure 14 (a) shows the initial state of the simulation indicating the geometry of the pattern. Figure 14 (b) shows the simulation of temperature fields for the current or "original" pattern geometry for the horizontal pattern. Blue areas at the upper end of the casting, which is the last section to fill, indicate the formation of cold laps or premature cooling of the melt front. This would indicate areas where there may be gaps or "misfilled" sections in the casting, which are consistent with actual defects observed in the pouring of ductile iron in the horizontal

pattern. Figure 14(c) shows simulated maximum sand temperatures. This simulation was performed to show where possible "sand penetration" defects might occur. The white and bright yellow areas nearest the center of the figure indicate areas of highest sand temperature and are likely to show the defect. It should be noted that this does not occur at 100% fill. Figure 14(d) shows simulation with venting. The simulation was performed to see how the formation of cold laps behaves with venting on top of the casting. Interestingly, the results seem to indicate that cold laps are still likely to be formed even with venting.

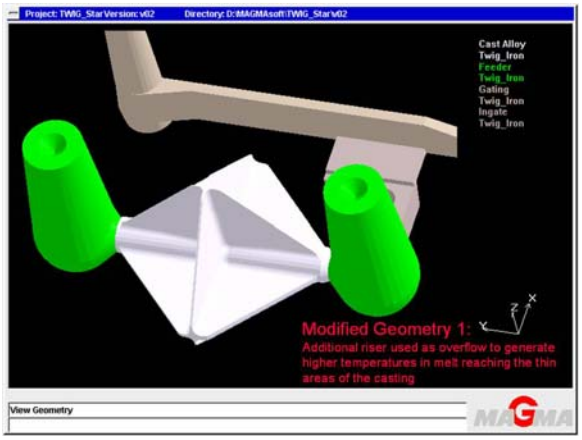

a) Geometry – No Simulation

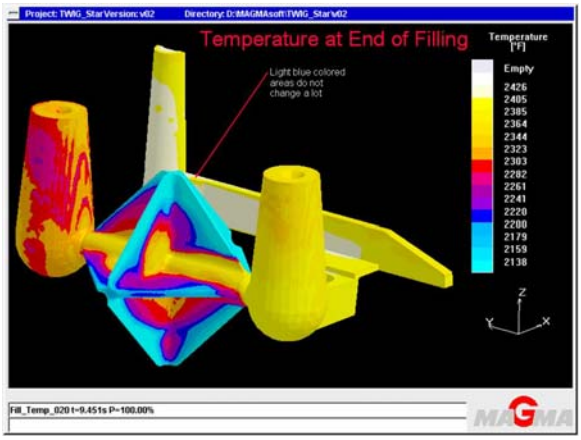

Temperature Field After Pouring

Figure 15: Pattern Geometry Proposal 1

Figure 15 (a) shows the first modified pattern geometry investigated. This configuration included an additional riser used as overflow to generate higher temperatures in melt reaching the thin areas of the casting. Figure 15 (b) shows the simulation of the temperature field for this modified pattern geometry. Although an additional riser was used, the formation of melt front temperature in the upper section of the castings appears to have changed little.

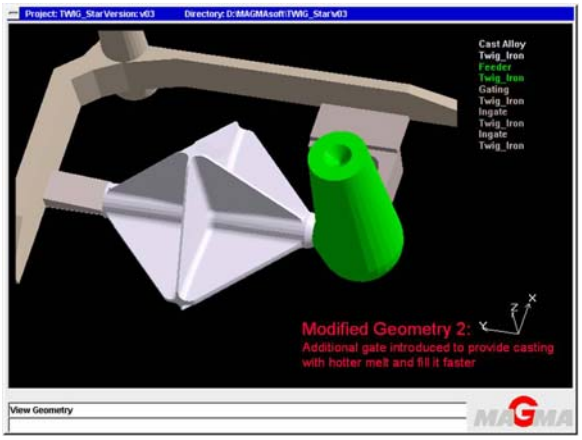

Geometry – No Simulation

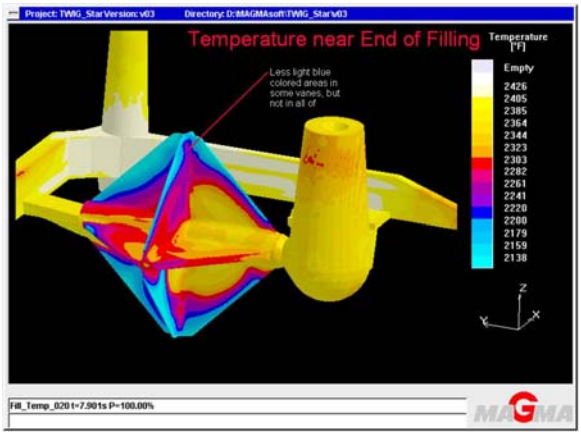

Temperature Field After Pouring

Figure 16: Pattern Geometry proposal 2

Figure 16 (a) shows a second geometry with an additional gate introduced to provide the casting with a hotter melt and to fill it faster. Figure 16 (b) shows the simulation of temperature fields showing the existence of cold front temperature at the upper end of the casting even with the additional gating.

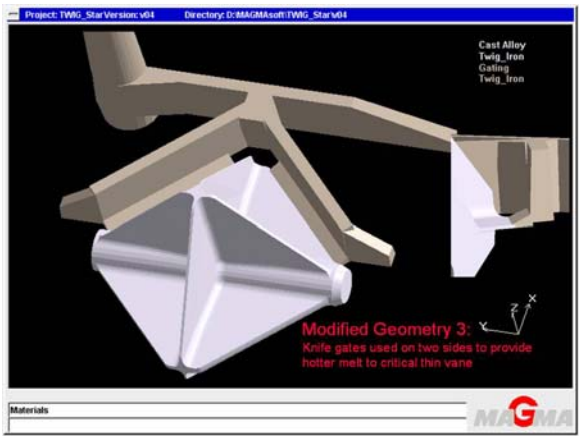

Geometry – No Simulation

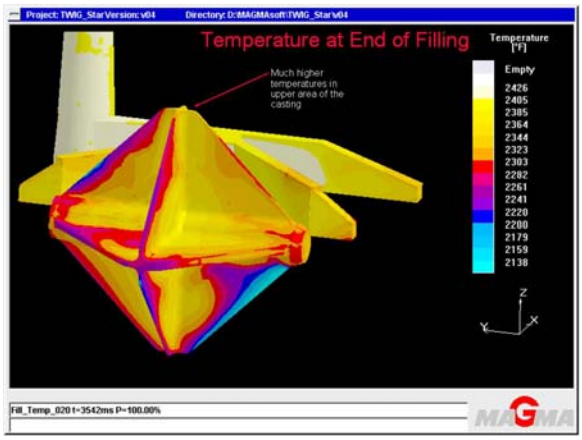

Temperature Field After Pouring

Figure 17: Pattern Geometry Proposal 3

The third geometry investigate is shown in Figure 17 (a), showing knife gates used on two sides to provide hotter melt to critical thin vane. It should be noted that the risers were not used in this proposed geometry. Figure 17 (b) shows the simulation of the temperature field indicating that much higher temperatures in upper area of the casting were obtained. This geometry shows promising results, but would also include more extensive cleanup of the castings.

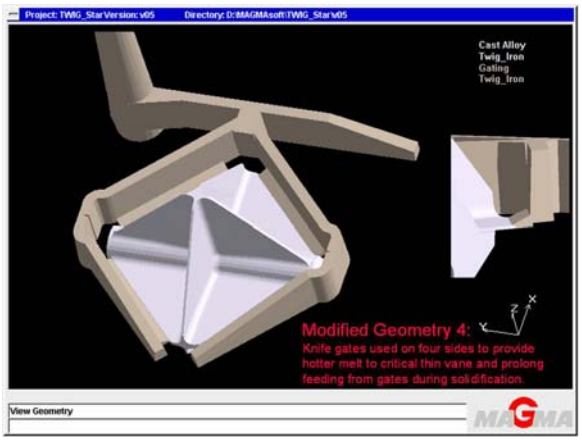

a) Geometry – No Simulation

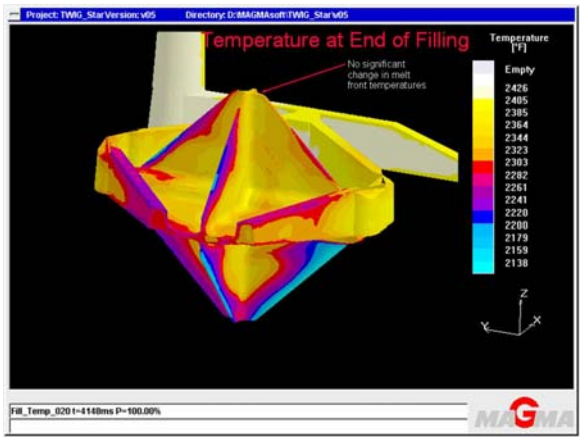

b) Temperature Field After Pouring

Figure 18: Pattern Geometry proposal 4

The fourth geometry proposed is shown in Figure 18 (a), showing knife gates used on four sides to provide hotter melt to the critical thin vanes and to prolong feeding from the gates during solidification. Figure 18 (b) shows the simulations of the temperature field. Using knife gates on two and four sides showed the highest melt front temperatures. However, the elimination of the riser led to a severe shrinkage defect in the casting because the liquid shrinkage could not be compensated through the thin ingates.

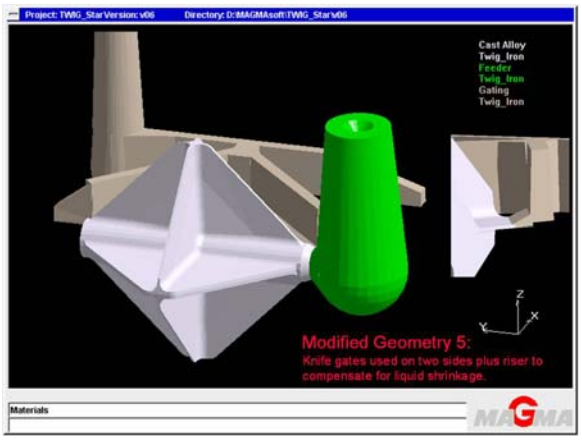

a) Geometry – No Simulation

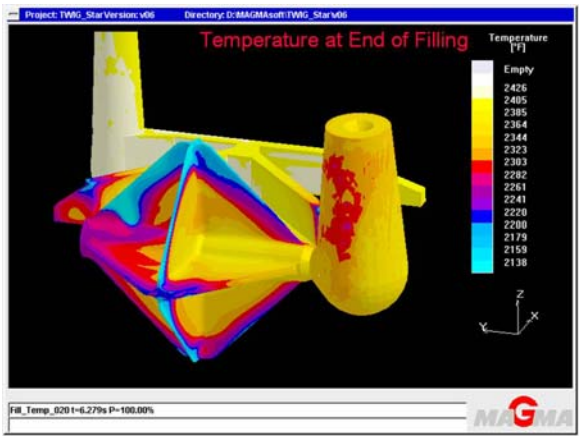

b) Temperature Field After Pouring

Figure 19: pattern Geometry Proposal 5

The final configuration investigated included a combination of the previous tests. Figure 19 (a) shows this geometry. Again, knife gates were used on two sides along with a riser to compensate for liquid shrinkage. Figure 19 (b) shows the simulations of the temperature field. The addition of the single riser to the knife gates shows lower melt front temperatures again, but they might be high enough to avoid cold laps.

Instrument Verification

Based on this methodology and given the relative accuracy of the CMM it is expected that gage R&R results for thickness measurements at each point will verify the assumption that most variation between parts is inherent with the parts.

The gage R&R study was evaluated at each point for thickness measurement. In total there were 129 point thicknesses evaluated. The study was based on two operators measuring ten parts in three trials. Analysis of percent variation components, i.e. repeatability and reproducibility were based on a 5.15 - sigma spread and values reported are averaged from results at each point. Table 4 shows the results from the gage R&R showing each process and its corresponding percent variation. The part-to-part variation is 99.79% which is much higher than variation due to equipment or operator. Figure 20 shows each operator's range for all 10 parts noting that this is also an average of 129 points for each part, and also includes the upper control limit (UCL) and average range for all parts. All the operator ranges are within the limit. The results clearly validate the assumption that most of the variation measured is a result of the variation inherent within the parts.

Table 4: Gage R&R Results

Process	% Variation
Repeatability (Equipment Variation)	4.4606%
Reproducibility (Appraiser Variation)	2.15683%
Gage R & R	5.26142%
Part-to-Part	99.78929%

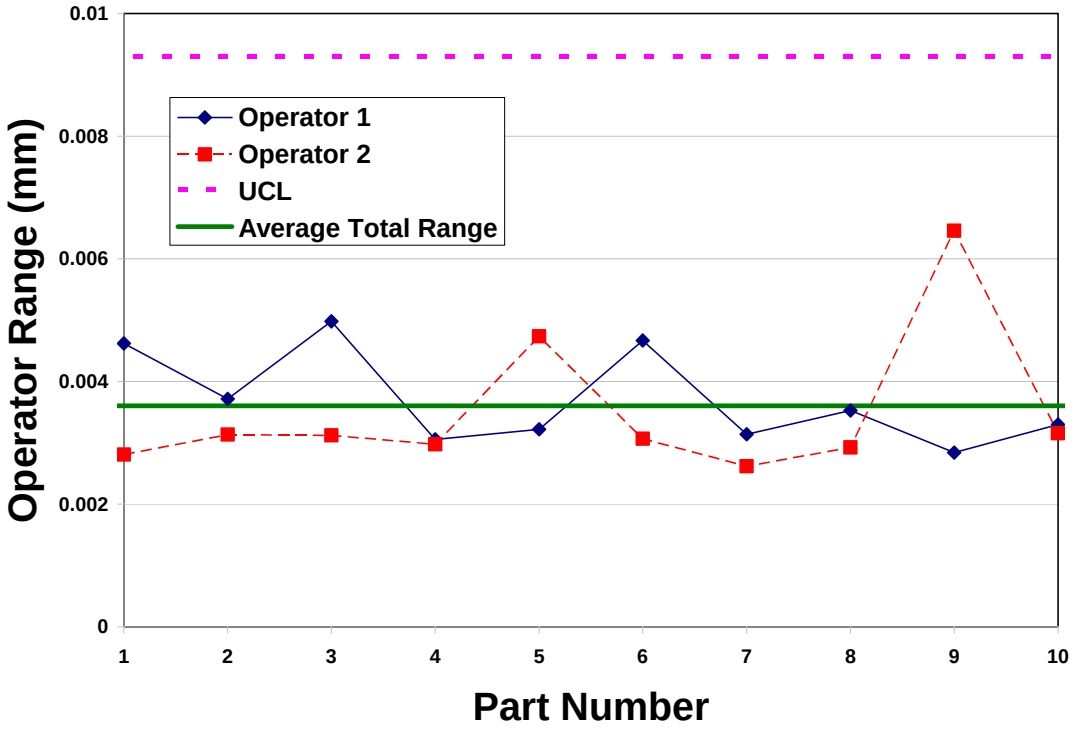

Figure 20: Operator Range for Gage R&R Study

Casting Round Robin

The patterns were circulated amongst the participating foundries in order to produce nominally 10 castings from each serial for a given set of test conditions. Rather than to dictate pouring conditions, the foundries were asked to provide the current conditions which were recorded. Some modifications were conducted at various foundries such as metal composition, but researchers did not ask for significant parameter variations such as sand temperature that would be invasive for the participants.

The cleaned castings were shipped to UNC Charlotte and preliminary data were collected using the techniques outlined earlier. Figure 21 shows a model of the vertically parting pattern to illustrate the numbering scheme for individual webs. The numbering scheme is similar for the horizontally parting pattern as well only the orientation is 90^{o} from vertical (i.e. webs 1,3,9,11 along the parting line are oriented horizontally instead of vertically).

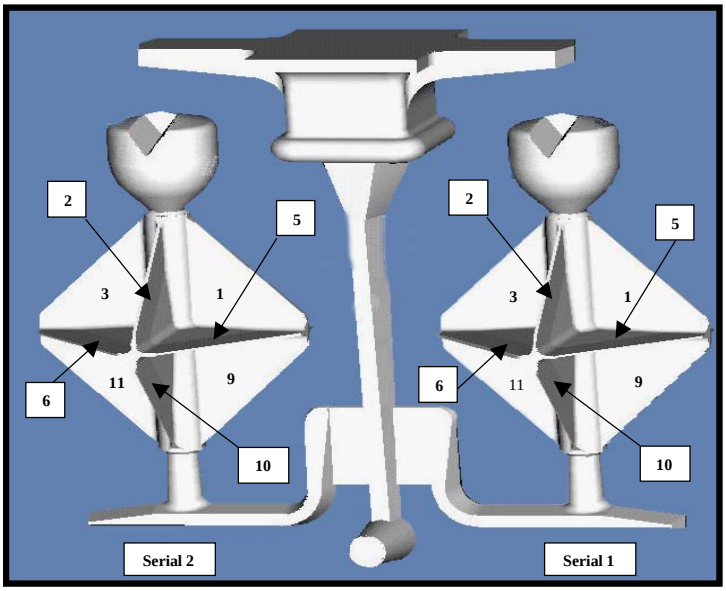

Front

A: Web Numbering, Front View

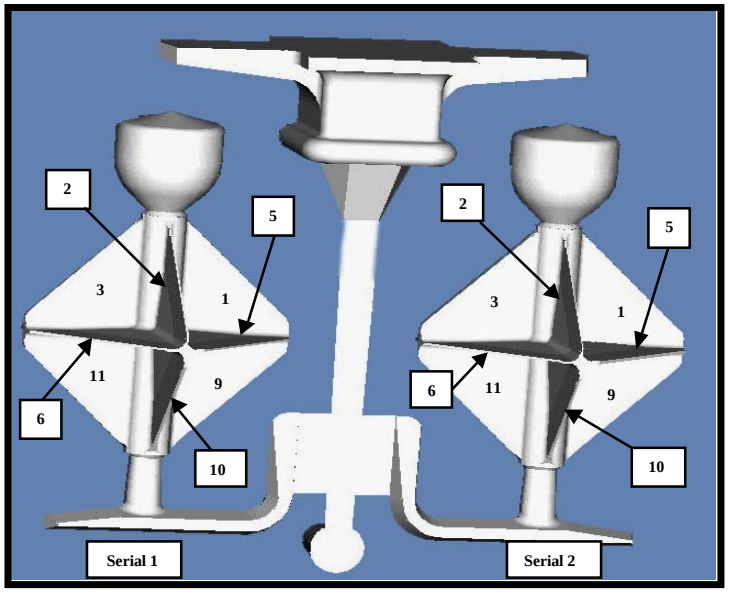

Rear

B) Web Numbering, Rear View

Figure 21: Web Numbering Scheme

Figure 22 shows the distribution of thickness values per web number ranging from approximately 1.5 mm to 6.32 mm. Webs 1,3,9, and 11 are located on the parting line.

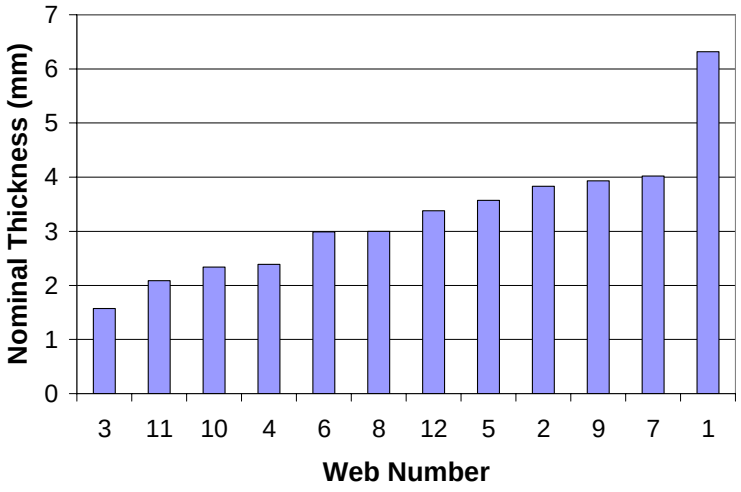

Figure 22: Thickness for Webs

Figure 23 shows the distribution of standard deviation of thickness values per web number. Four of the six thickest webs have standard deviation values above 0.25 mm while the thinnest webs are primarily below 0.20 mm.

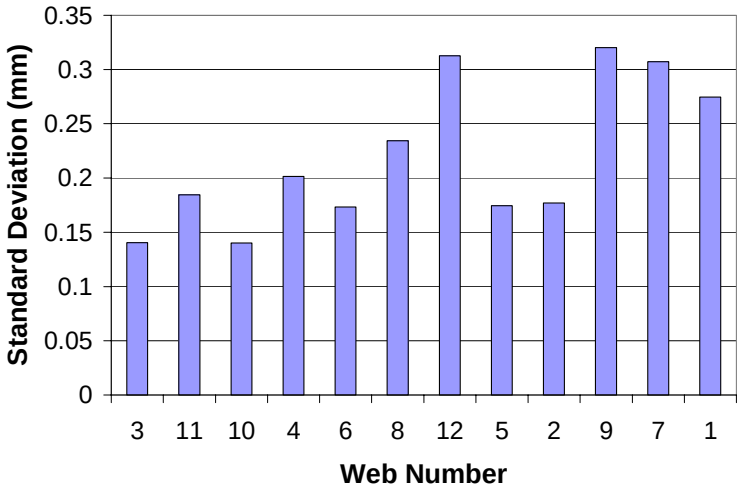

Figure 23: Standard Deviation for Webs Arranged by Thickness

Figure 24 is a similar distribution of standard deviation values with serial 1 and serial 2 values Segregated. With the exception of web 4 and web 5, serial 1 has lower standard deviation (average of all: 0.209 mm) than serial 2 (average of all 0.242 mm). The maximum difference in standard deviation between serial 1 and serial 2 occurs on web 7 with serial 1 less by 0.066 mm. The minimum difference occurs at web 4 with serial 2 less by 0.003 mm.

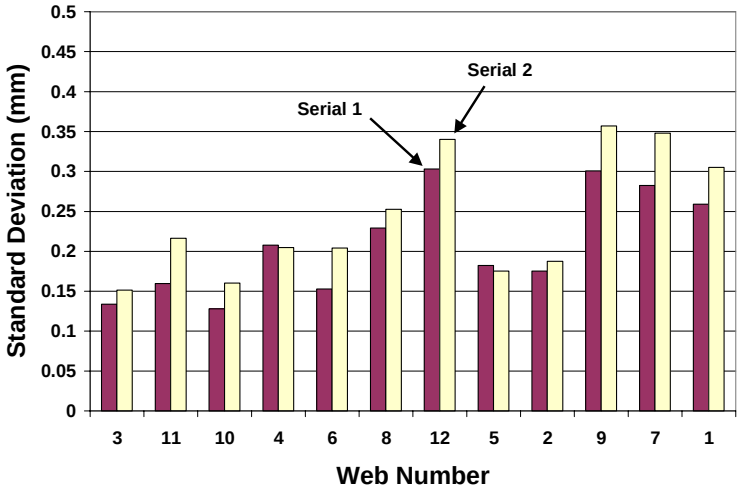

Figure 24: Serial 1 vs. Serial 2 Web Standard Deviation

Figure 25 is a side by side comparison of horizontal and vertical web data. This illustrates the large difference in standard deviation values between the two (vertical average: 0.0644 mm, horizontal average: 0.290 mm).

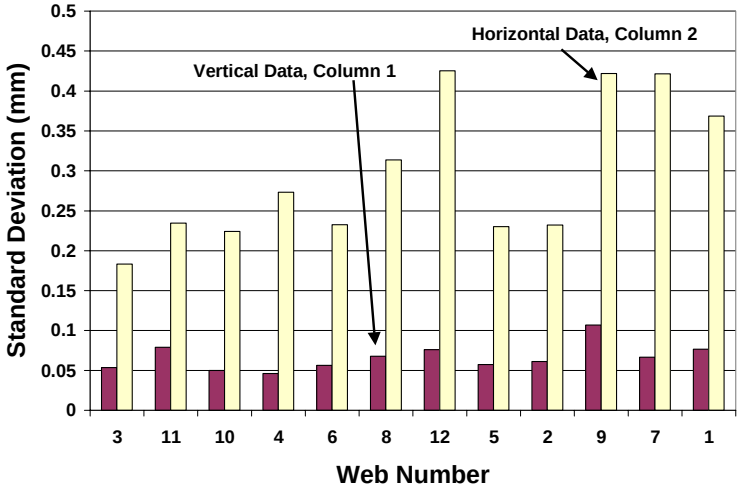

Figure 25: Vertical, Horizontal Pattern Web Standard Deviation

Further analysis of the serial 1 and serial 2 data, this time segregated further by pattern type shown in Figure 26 indicates that the vertical pattern is less dependent on serial number than the horizontal data. In Figure 26A, the vertical standard deviation values for serial 1 and serial 2 are more or less randomly distributed. Figure 26B however follows the same pattern as the average of both pattern types with serial 1 primarily having less standard deviation than serial 2.

The inferences from this analysis is that the horizontally parting pattern yield standard deviation values that are more dependent on placement in the mold, i.e. the thinner webs placed closer to the feed sprue (webs 3, 11) have less variation than when they are oriented near the outer edge of the mold. Contrasting that, the thicker webs (webs 1,9) placed closer to the edge of the mold tend to have less variation than those placed closer to the gating. The inferences with respect to the vertically parted pattern and mold placement are harder to make since standard deviation is less in serial 2 for webs 1,9, and 11 and more for web 3.

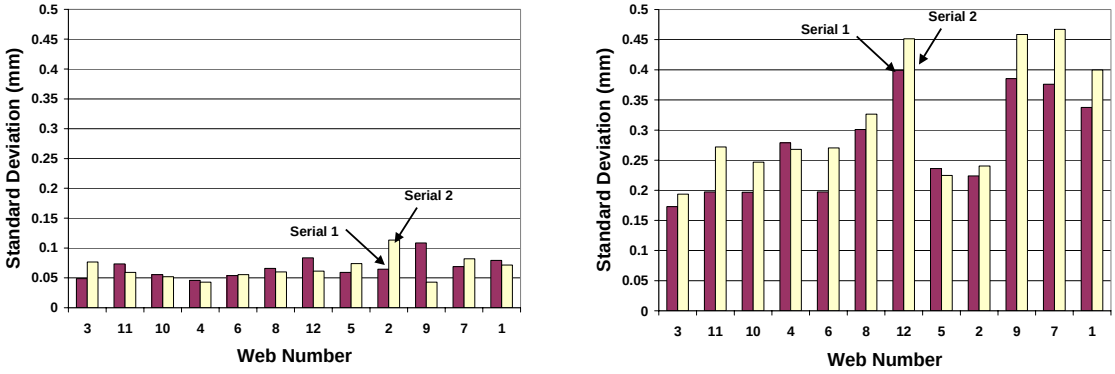

A) Vertical Pattern, Serial 1 and Serial 2 B) Horizontal Pattern, Serial 1 and Serial 2

Figure 26: Vertical and Horizontal Pattern Web Standard Deviation Values per Web, Segregated Serial 1 and Serial 2 Values

Parametric Study

All of the parameters recorded during the pouring of castings are shown in Figure 27 through Figure 29, with standard deviaiton (mm) of thickness shown on the Y-axis. Where appropriate a linear best fit line is applied with R^2 values shown. The horizontal (diamonds, higher standard deviation values) and vertical data (circles, lower standard deviation values) are highlighted for convenience of viewing on all plots except Side, Pattern Type, and Iron Type.

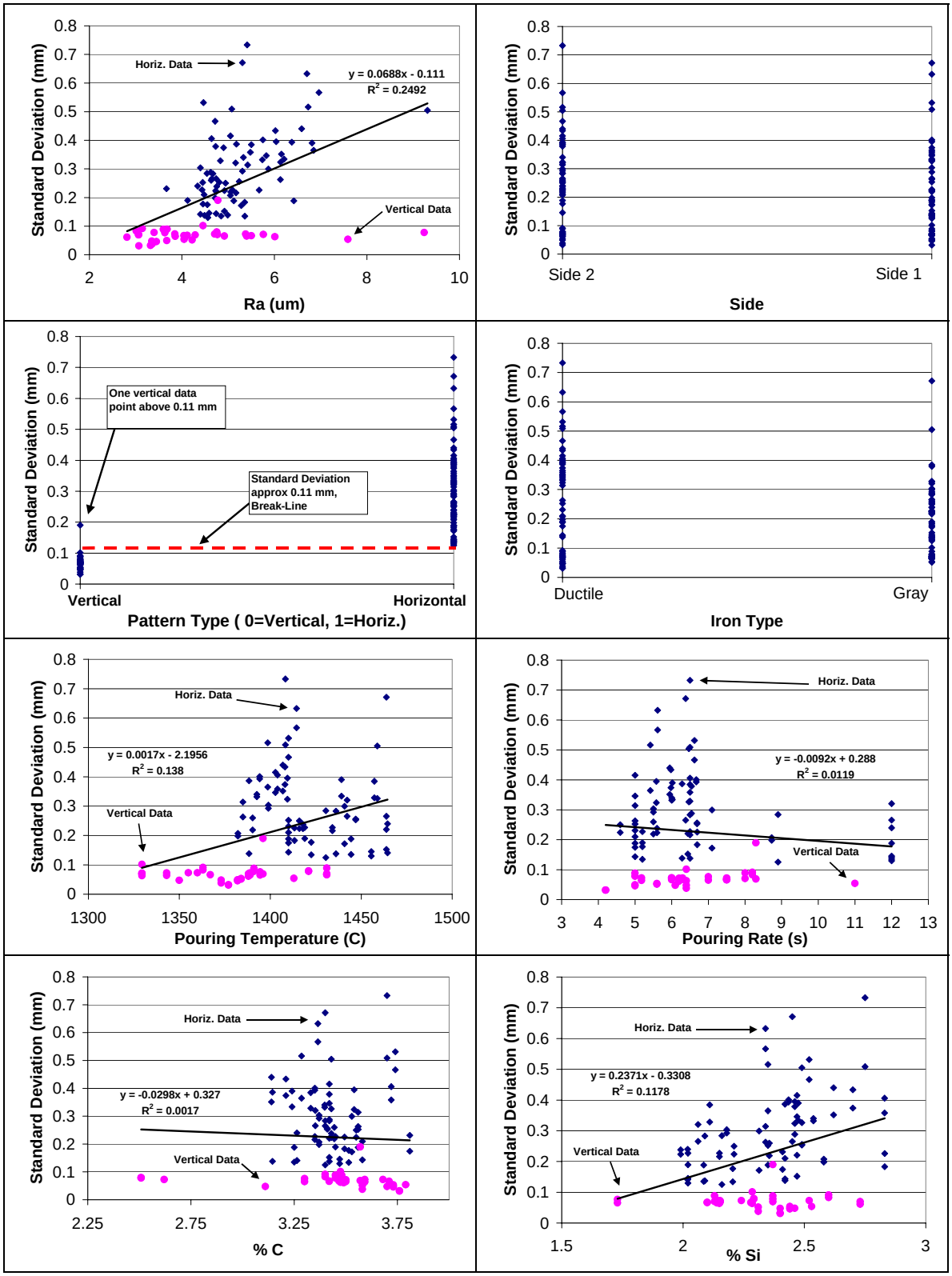

Figure 27: Standard Deviation vs. Each Parameter

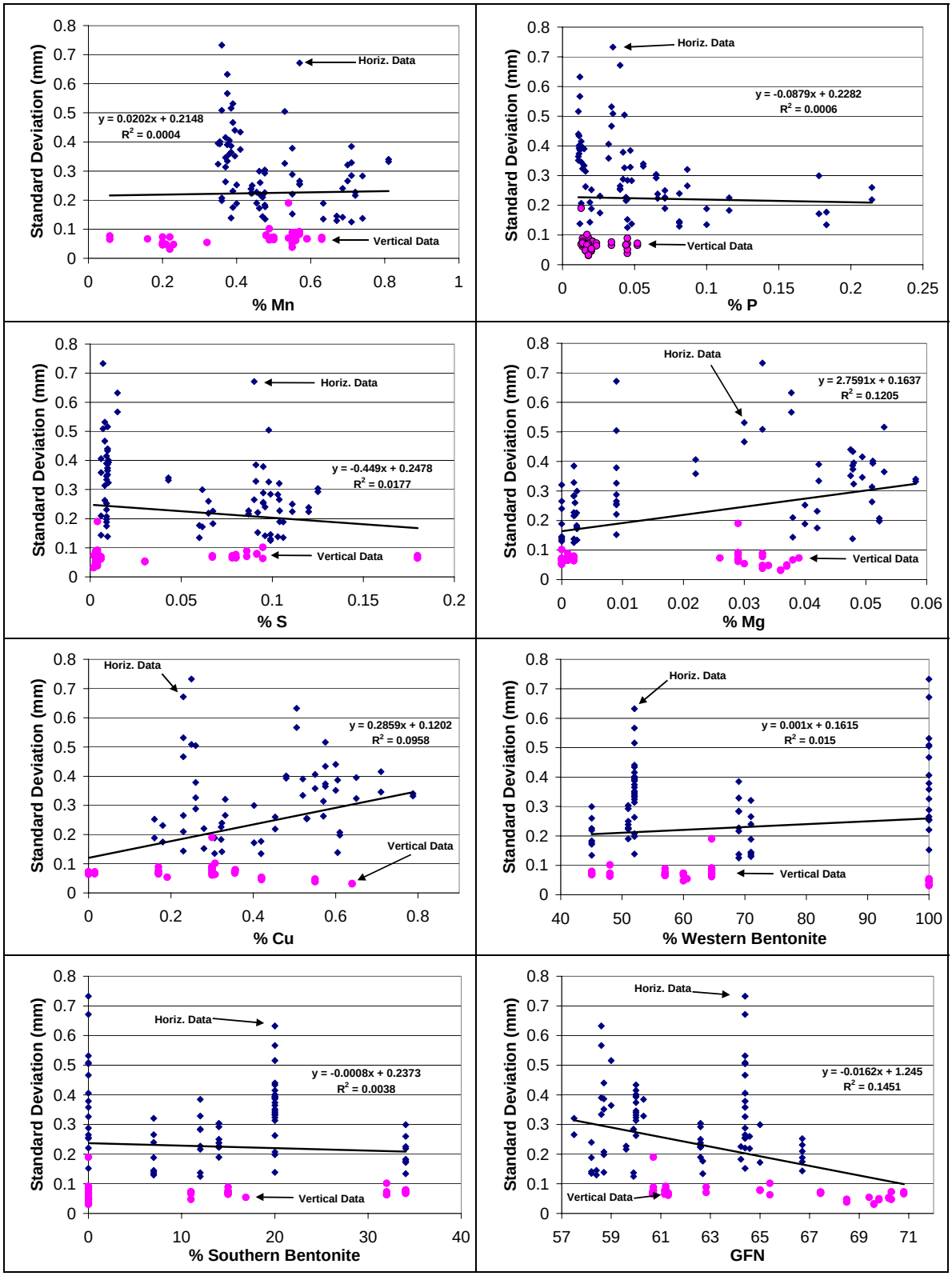

Figure 28: Standard Deviation vs. Each Parameter

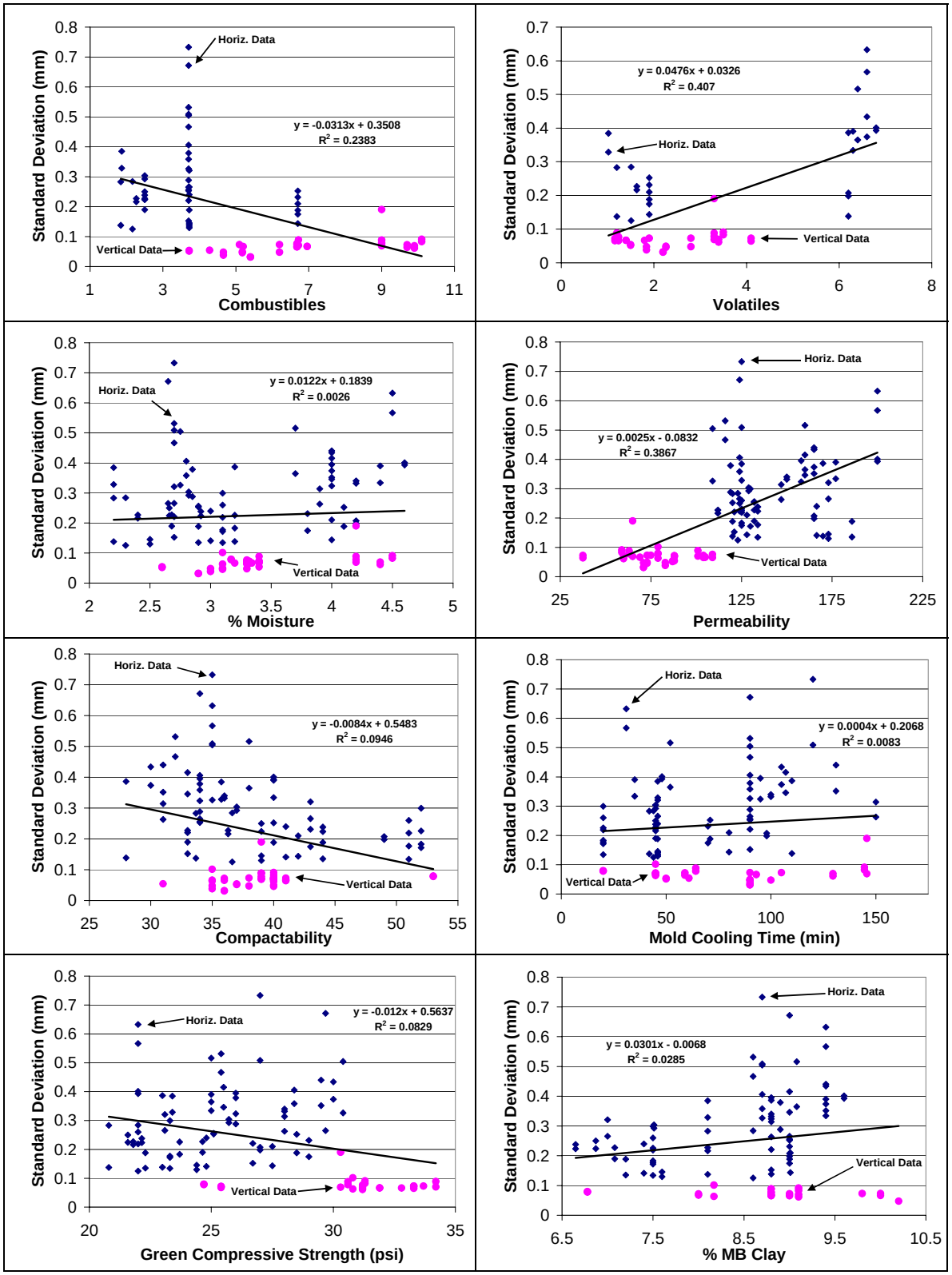

Figure 29: Standard Deviation vs. Each Parameter

All of the plots show very poor linear relationships between the parameters and standard deviation of thickness with no R^2 values above 0.407, and most well below that number. Although not shown, similar conclusions can be made about the vertically parted and horizontally parted pattern data which also show a poor linear relationship to standard deviation of thickness. The attempt to interpret this data in some meaningful way, will be by way of statistical regresssion. In doing so we will attempt to find a relationship between certain combinations of the parameters or subsets of the parameters.

Statistical Regression Analysis

In order to determine the parametric influences on variation in the thin features cast, a linear regression analysis was carried out using SAS Release 8.02, statistical analysis software. The standard deviation values used to represent the variation present in thickness measurements were averaged per casting from a total of 129 individual point measurements per casting. The regression model, as will be shown, required that the number of parameters considered be narrowed to subsets of the total parameter set.

Due to the significant difference in variations between those castings poured on vertical and horizontal machines, multiple analyses were conducted including a) "Full Model" including all data, b) data from Vertical machines, and c) data from Horizontal machines. Each are discussed below.

Full Model

The initial regression model based on all parameters (except Mold Cooling Time, Combustibles, and Volatiles - removed due to the low number of available observations) is shown in Table 5 and Figure 30 through Figure 32 for residuals, predicted value of standard deviation, and the normal probability plot. In interpreting these plots, the **desired response** for the residuals (Figure 30) is a "shotgun" plot, with data randomly placed throughout the plot area. This would indicate that the regression had been successful at identifying all repeatable trends and only random noise remains. The regression shown in Figure 31 would ideally be linear with a slope of one. Figure 31 approaches this, but has spread in the data and a curvilinear shape indicating that a parameter has not been fully modeled. The data in Figure 32 should also be linear, indicating normal distribution of the data collected.

Table 5: SAS Linear Regression Output for Full Model

Analysis of Variance					
Source	DF	Sum of Squares	Mean Square	F Value	Pr > F
Model	21	1.56958	0.07474	9.79	<.0001
Error	47	0.35868	0.00763		
Corrected Total	68	1.92826			

Root MSE	0.08736	R-Square	0.8140
Dependent Mean	0.26802	Adj R-Sq	0.7309
Coeff Var	32.59449		

Parameter Estimates						
Variable	DF	Parameter Estimate	Standard Error	t Value	Pr > |t|	Variance Inflation
Intercept	1	-1.01779	1.43308	-0.71	0.4811	0
Ra	1	0.03501	0.01617	2.17	0.0355	2.71153
Side	1	-0.02769	0.02111	-1.31	0.1959	1.00678
Pattern_Type	1	0.56582	0.29432	1.92	0.0606	151.02046
Iron_Type	1	-0.80609	0.29960	-2.69	0.0098	202.51335
Pouring_Temp	1	-0.00098073	0.00104	-0.94	0.3503	10.24565
Pouring_Rate	1	-0.03213	0.01999	-1.61	0.1147	11.75143
C	1	-0.08516	0.14715	-0.58	0.5656	3.89066
Si	1	-0.24782	0.14670	-1.69	0.0978	11.56404
Mn	1	0.23277	0.17897	1.30	0.1997	5.37588
Ph	1	-1.01191	0.94994	-1.07	0.2922	21.87516
S	1	3.82963	2.39318	1.60	0.1163	75.76306
Mg	1	-9.70919	5.41269	-1.79	0.0793	119.68679
Cu	1	-0.40579	0.14644	-2.77	0.0080	6.04367
Western_Bentonite	1	-0.01293	0.01050	-1.23	0.2243	361.83950
Southern_Bentonite	1	-0.01661	0.01311	-1.27	0.2114	213.08315
GFN	1	0.05834	0.02625	2.22	0.0311	42.79199
Moisture	1	-0.11001	0.10227	-1.08	0.2876	36.90057
Permeability	1	0.00213	0.00173	1.23	0.2232	37.91934
Compactability	1	0.00737	0.00631	1.17	0.2487	14.60159
Green_Comp	1	0.01237	0.00944	1.31	0.1964	9.81925
MBClay	1	0.08025	0.09808	0.82	0.4173	42.40019

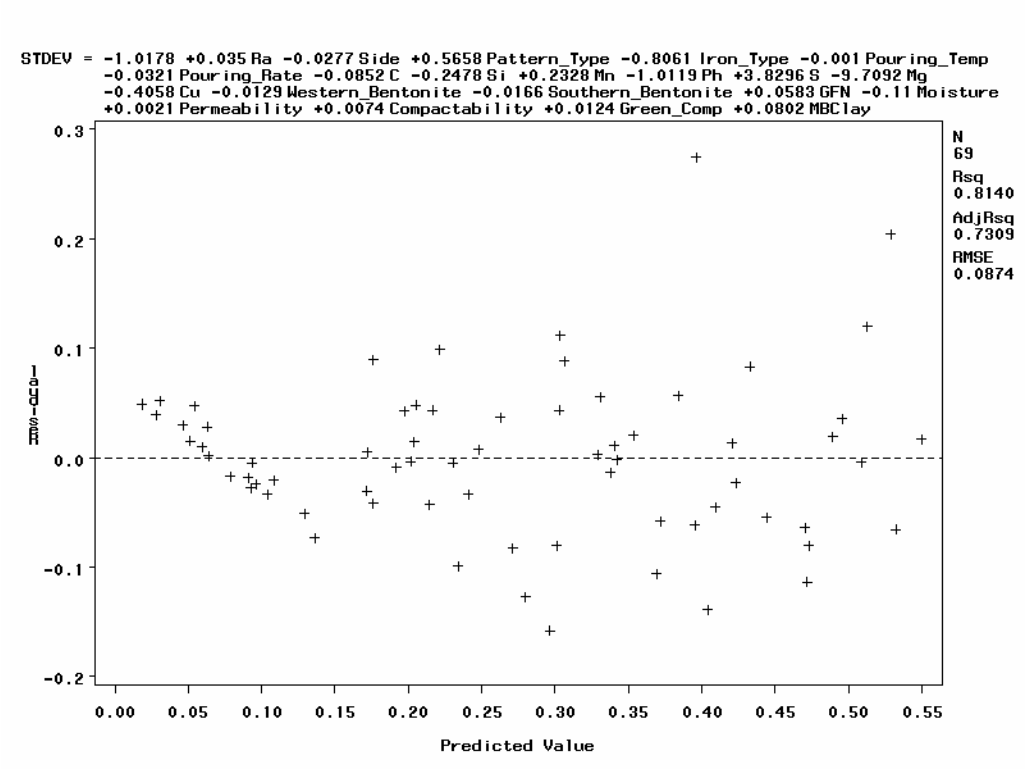

Figure 30: Residuals for Full Model

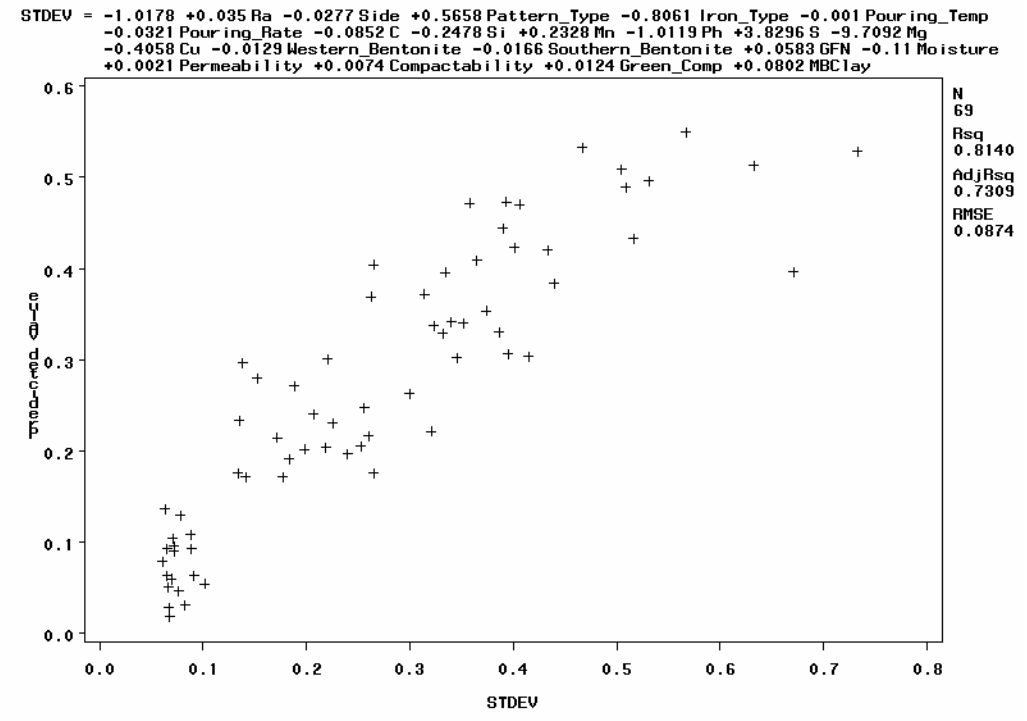

Figure 31: Regression for Standard Deviation (mm), Full Model

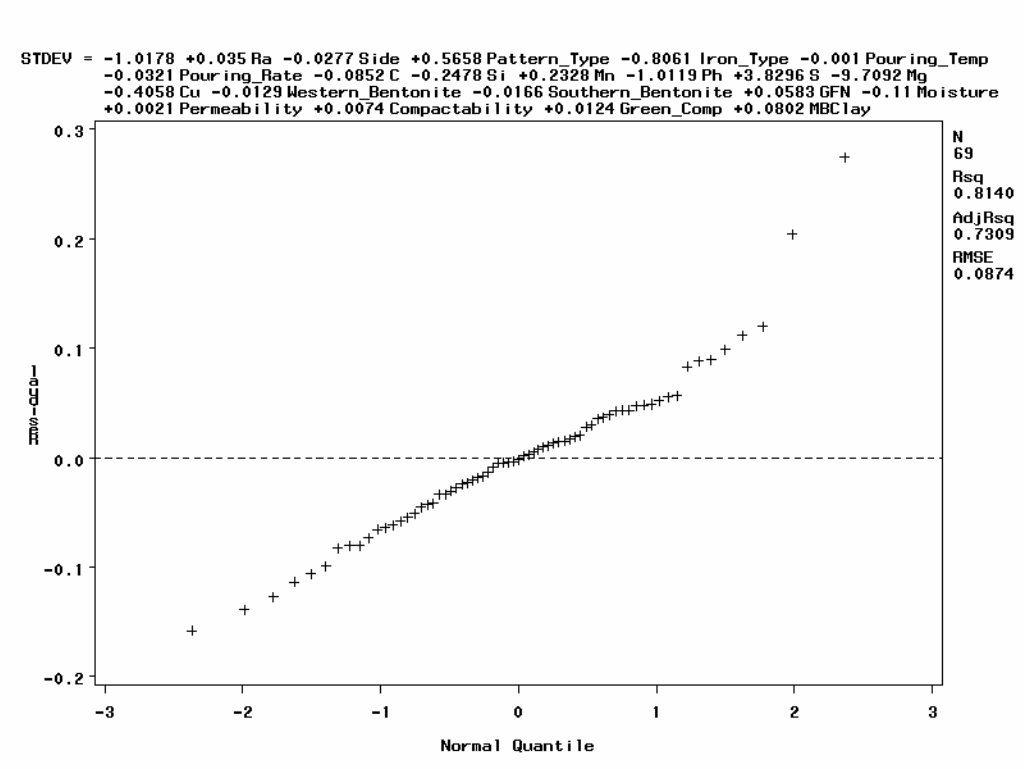

Figure 32: Normal Probability Plot, Full Model

The table of regression coefficients shows that *p-values* are very high for all of the parameters in the model. Although conventions vary, *p-values* of less than 0.05 are typically indicative that the particular parameter has a strong influence on the effect being measured. This indicator, along with the large number of observations (69) means that a subset of the full model is required. To find the subset(s) an automatic search function in SAS (R Square Selection Method) was used. The function calculates the R^2 value for all combinations of parameters and simultaneously determines the C_p values which is an indicator of bias in the model. The goal is to find an unbiased model with as few parameters (predictors) as possible, while attempting to maintain a good R^2 value. Table 18 in the appendix shows the SAS output for the R^2 Selection.

When attempting to select a subset from Table 18, the R^2 values were not consistent. This was due to some missing data for certain observations. Therefore, when subsets were selected the regression changed, making it difficult to rely on the selection procedure. In order to stabilize the procedure two parameters for which several observations had missing values were removed, namely MB Clay and Green Compressive Strength. Table 19 in the appendix shows the selection procedure again with the modified data set.

The subset including Ra Pattern_Type Iron_Type Pouring_Temp Pouring_Rate Mn Ph Mg Cu Western_Bentonite Permeability with 11 parameters was chosen and then regressed to check the coefficients.

Table 6: SAS Linear Regression Output for Initial Subset

Analysis of Variance					
Source	DF	Sum of Squares	Mean Square	F Value	Pr > F
Model	11	1.98994	0.18090	27.27	<.0001
Error	72	0.47755	0.00663		
Corrected Total	83	2.46749			

Root MSE	0.08144	R-Square	0.8065
Dependent Mean	0.23136	Adj R-Sq	0.7769
Coeff Var	35.20154		

Parameter Estimates						
Variable	DF	Parameter Estimate	Standard Error	t Value	Pr > |t|	Variance Inflation
Intercept	1	0.96898	0.57292	1.69	0.0951	0
Ra	1	0.03537	0.01057	3.35	0.0013	1.90100
Pattern_Type	1	0.24565	0.04701	5.23	<.0001	6.67450
Iron_Type	1	-0.23523	0.06535	-3.60	0.0006	13.45274
Pouring_Temp	1	-0.00059535	0.00045094	-1.32	0.1909	2.99967
Pouring_Rate	1	-0.02968	0.00751	-3.95	0.0002	2.34643
Mn	1	0.14932	0.07877	1.90	0.0620	1.62177
Ph	1	-0.55291	0.32123	-1.72	0.0895	3.02858
Mg	1	-4.23006	1.96781	-2.15	0.0349	20.57057
Cu	1	-0.33156	0.08990	-3.69	0.0004	3.29371
Western_Bentonite	1	0.00136	0.00067252	2.02	0.0466	2.48116
Permeability	1	0.00144	0.00059229	2.42	0.0179	7.73516

Noting that Mg and Iron type have moderately high variance inflation numbers (above 11.0, indicating multicollinearity), the subset selection was rerun without Magnesium (Mg is relatively high or low depending on the iron type, Ductile or Gray): The results are shown in the appendix under Table 20.

Two subsets were selected with R^2 values approaching 0.8 and containing 11 parameters. It is noteworthy that many of the variables in these subsets appear consistently throughout the table. A second subset was selected since it is similar to the first and compactability appears which likely has some affect on part variation. Note that Side (symbol indicating serial number) appears in these subsets, when Magnesium (Mg) was removed from consideration.

Subsets:

1) Ra Side Pattern_Type Iron_Type Pouring_Temp Pouring_Rate Mn Ph Cu Western_Bentonite Permeability

2) Ra Side Pattern_Type Iron_Type Pouring_Temp Pouring_Rate Mn Cu Western_Bentonite Permeability Compactability

The subsets were then regressed to check the coefficients for subset 1 (see Table 7, Figure 33, Figure 34, and Figure 35) and subset 2 (see Table 8, Figure 36, Figure 37, and Figure 38).

Subset 1:

Table 7: SAS Linear Regression Output for Subset 1

Analysis of Variance					
Source	DF	Sum of Squares	Mean Square	F Value	Pr > F
Model	11	1.96756	0.17887	25.76	<.0001
Error	72	0.49993	0.00694		
Corrected Total	83	2.46749			

Root MSE	0.08333	R-Square	0.7974
Dependent Mean	0.23136	Adj R-Sq	0.7664
Coeff Var	36.01701		

Parameter Estimates						
Variable	DF	Parameter Estimate	Standard Error	t Value	Pr > |t|	Variance Inflation
Intercept	1	1.03774	0.58548	1.77	0.0805	0
Ra	1	0.03433	0.01082	3.17	0.0022	1.90188
Side	1	-0.01990	0.01824	-1.09	0.2789	1.00612
Pattern_Type	1	0.22793	0.04738	4.81	<.0001	6.47775
Iron_Type	1	-0.10923	0.02870	-3.81	0.0003	2.47799
Pouring_Temp	1	-0.00075453	0.00045476	-1.66	0.1014	2.91404
Pouring_Rate	1	-0.02396	0.00724	-3.31	0.0015	2.08289
Mn	1	0.12257	0.07979	1.54	0.1289	1.58963
Ph	1	-0.24983	0.29578	-0.84	0.4011	2.45267
Cu	1	-0.40527	0.08506	-4.76	<.0001	2.81700
Western_Bentonite	1	0.00184	0.00064549	2.85	0.0056	2.18338
Permeability	1	0.00130	0.00060267	2.16	0.0341	7.65015

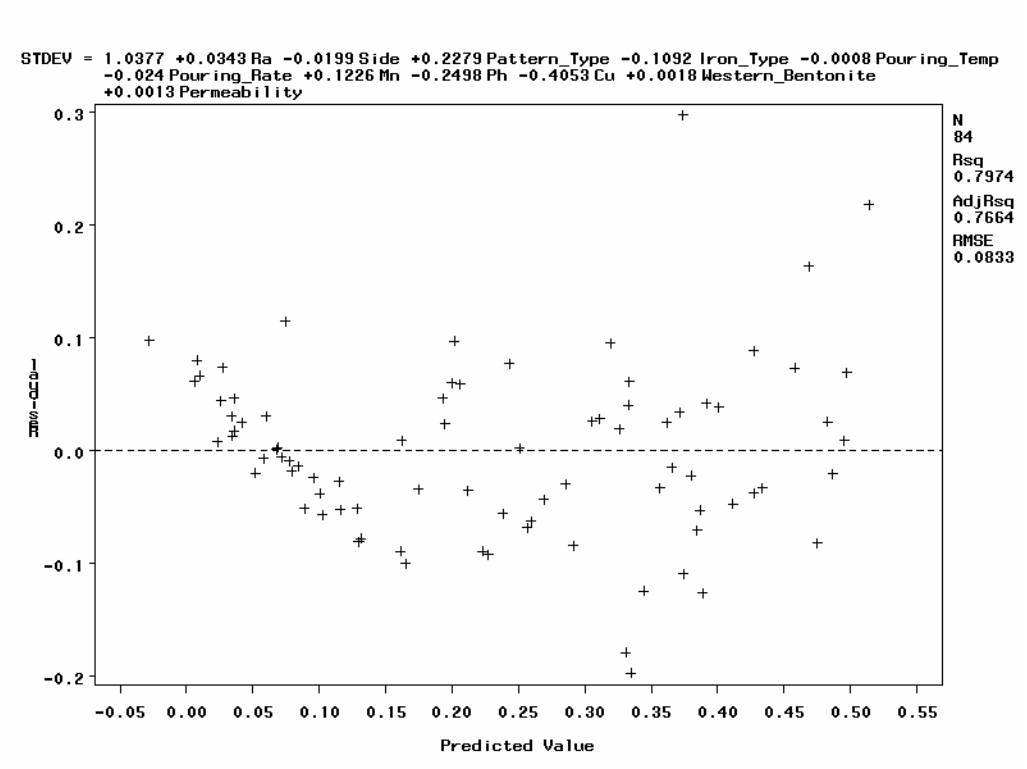

Figure 33: Residuals for Full Model Subset 1

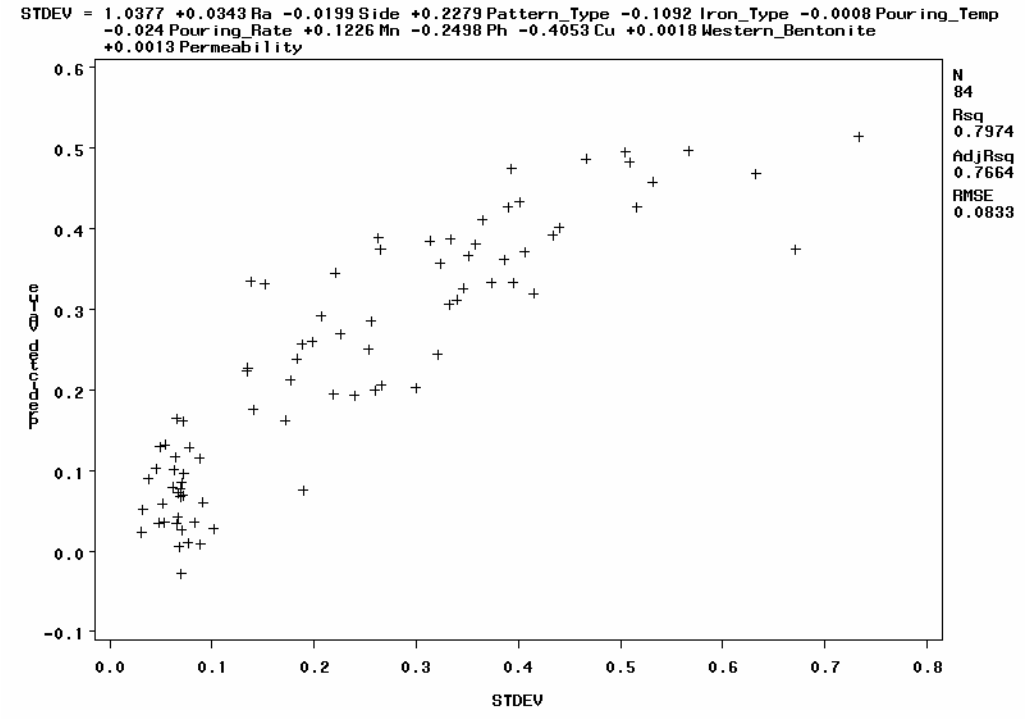

Figure 34: Regression for Standard Deviation (mm), Full Model Subset 1

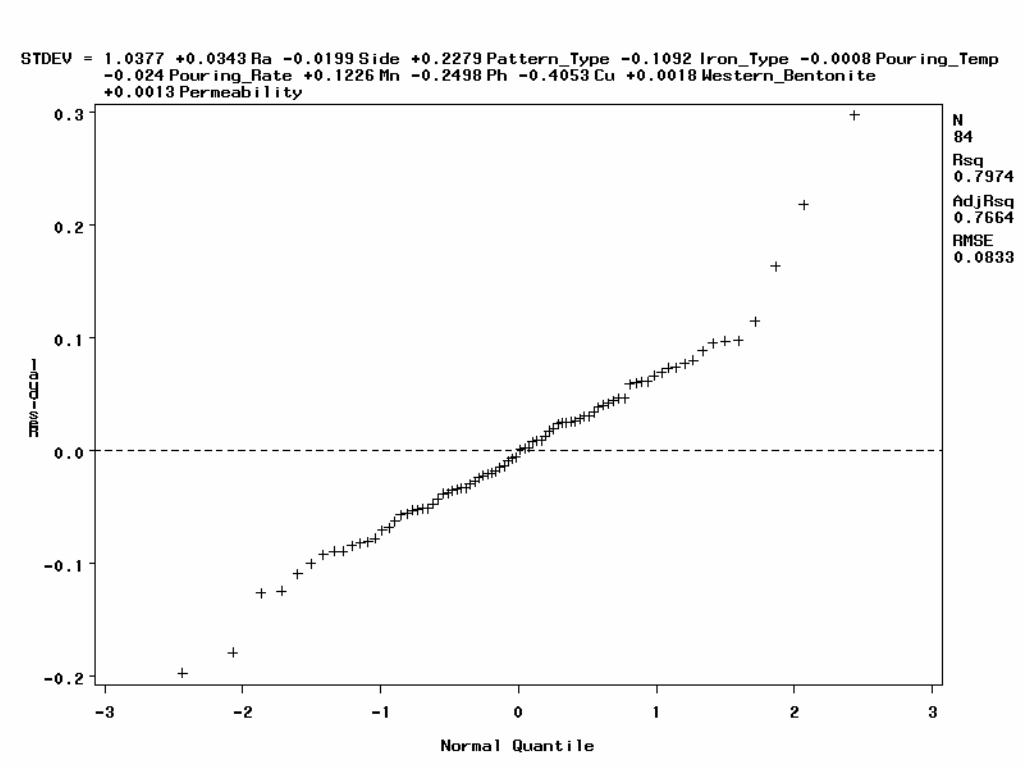

Figure 35: Normal Probability Plot, Full Model Subset 1

Subset 2:

Table 8: SAS Linear Regression Output for Full Model Subset 2

Analysis of Variance					
Source	DF	Sum of Squares	Mean Square	F Value	Pr > F
Model	11	1.96675	0.17880	25.71	<.0001
Error	72	0.50074	0.00695		
Corrected Total	83	2.46749			

Root MSE	0.08340	R-Square	0.7971
Dependent Mean	0.23136	Adj R-Sq	0.7661
Coeff Var	36.04621		

Parameter Estimates						
Variable	DF	Parameter Estimate	Standard Error	t Value	Pr > |t|	Variance Inflation
Intercept	1	1.15816	0.57315	2.02	0.0470	0
Ra	1	0.03409	0.01099	3.10	0.0027	1.96087
Side	1	-0.02047	0.01826	-1.12	0.2662	1.00723
Pattern_Type	1	0.21913	0.04353	5.03	<.0001	5.45879
Iron_Type	1	-0.11514	0.02575	-4.47	<.0001	1.99188
Pouring_Temp	1	-0.00079755	0.00044548	-1.79	0.0776	2.79188
Pouring_Rate	1	-0.02320	0.00750	-3.09	0.0028	2.23299
Mn	1	0.11494	0.08227	1.40	0.1667	1.68717
Cu	1	-0.41095	0.08410	-4.89	<.0001	2.74931
Western_Bentonite	1	0.00179	0.00069187	2.59	0.0117	2.50434
Permeability	1	0.00135	0.00058768	2.30	0.0244	7.26242
Compactability	1	-0.00165	0.00214	-0.77	0.4428	1.91908

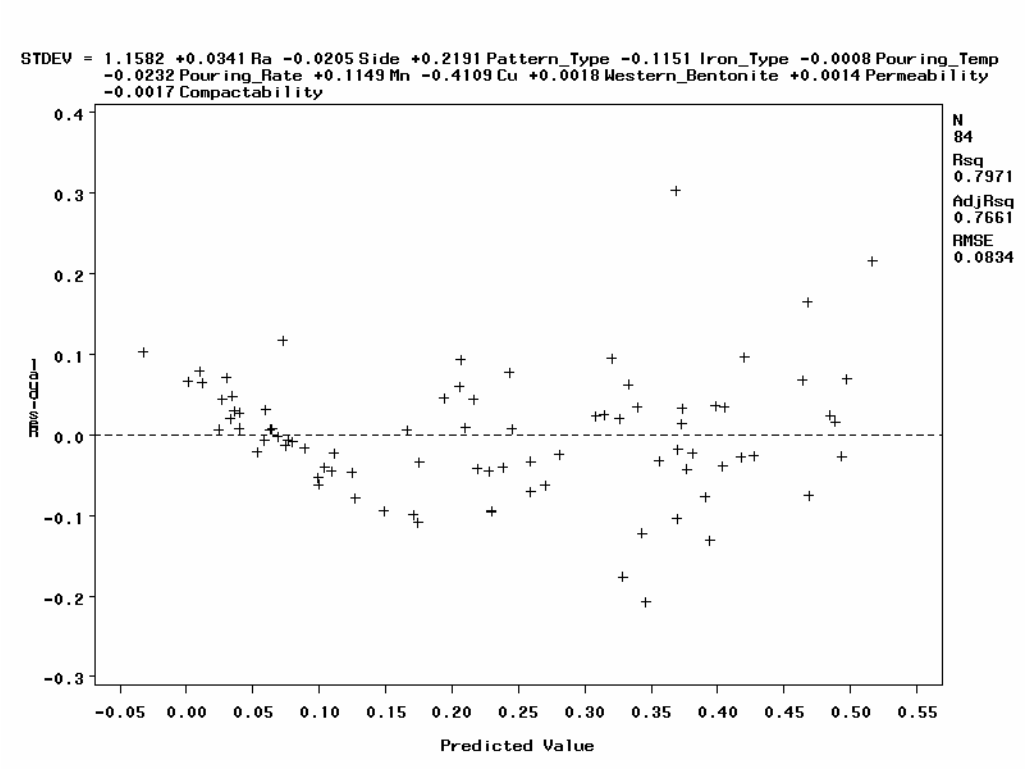

Figure 36: Residuals for Full Model Subset 2

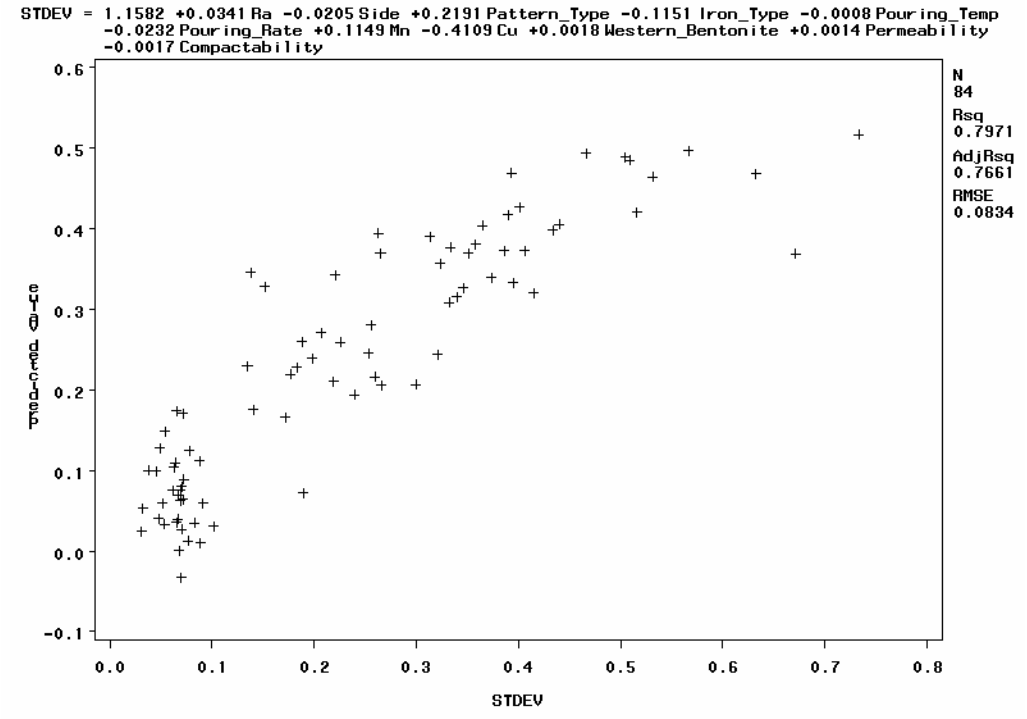

Figure 37: Regression for Standard Deviation (mm), Full Model Subset 2

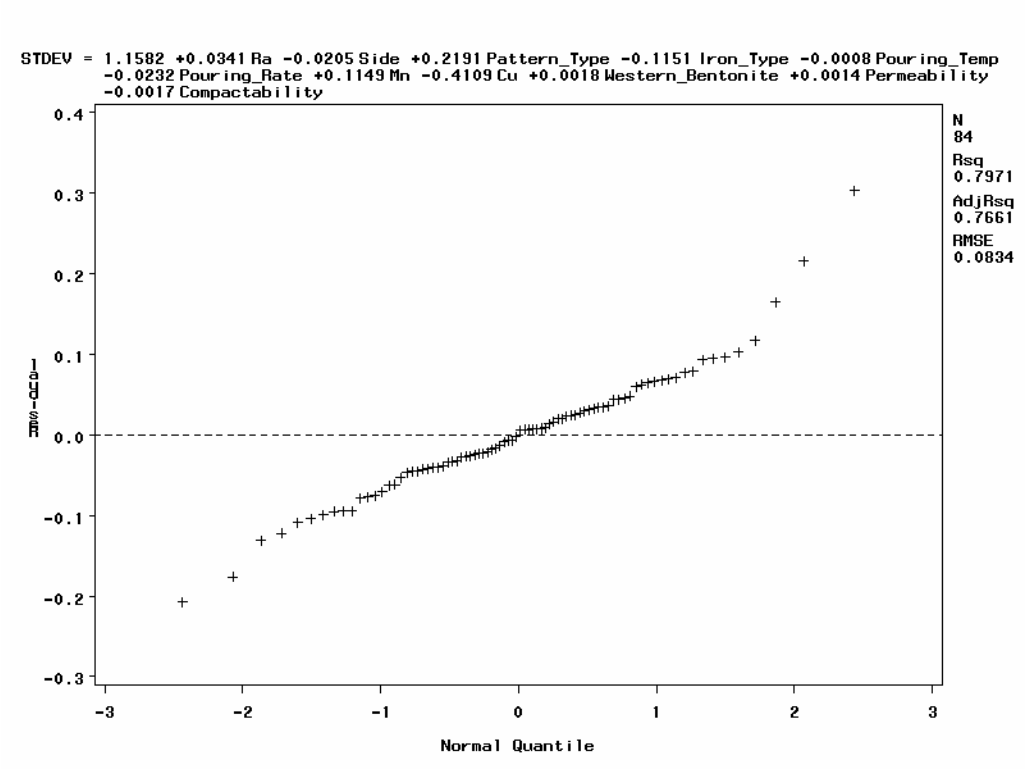

Figure 38: Normal Probability Plot, Full Model Subset 2

In both subsets R^2 approaches 0.8 and variance inflation for each variable is low while Side, Mn, Phos., Compactability, permeability, and western bentonite have the highest P-values (noting that several variables have $P > 0.001$. Reducing the number of variables further will also decrease the R^2 value, thus reducing the appropriatness of the fit. More importantly however, there is a notable departure from normality, indicated in the residuals plots and to some degree in the normal probability plots. Additionally, there is an apparent nonlinearity in the regression plots. In the residuals plots it is evident that parts with the lowest variation appear to have a regression of differing slope from those with higher variation. This seperation is consistent with parts poured in the vertically seperated mold (lower standard dev.) and those poured in horizontally parted molds (higher standard dev.). Ideally, regression terms, specifically qualitative variables with interaction effects e.g. parameter *pattern_type*, would be included in the model. However, the relatively low number of observations, i.e. low number of degrees of freedom, prohibits using these interaction terms that would allow the model to compensate for the varied slopes.

Vertical Model

Noting the regression slope discontinuity created when the vertical and horizontal pattern data are regressed together, the data was segregated and regressed separately for the vertical and horizontal molding machines. For the vertical data it was again necessary to select a subset of parameters to get a model with improved P-values. The SAS R Squared Selection procedure was used (results not shown) and several subsets ranging from six to eight variables were selected for further analysis. A seven parameter subset was selected as the best fit, the results are shown in Table 9 and Figure 39 through Figure 41.

The seven variable subset (Side Pouring_Rate Si Mn Ph S Southern_Bentonite) had the highest R^2 value at 0.5713 and exhibited the best P-values. Additionally, the variance inflation factors were all below 11.0 indicating that multicollinearity is not likely an issue. Two variables, Sulfur and percent Southern Bentonite did have relatively high P-values. Removing them from the model does however affect the model adversely,

reducing the R^2 value and increasing P-values for the remaining variables in the model. The residual plot as well as the regression plot do not indicate any apparent nonconstant error variance or nonlinearity, however the normal probability plot does indicate some problems with the normality of the fit.

7 Parameter Subset, Vertical Data only:
Side Pouring_Rate Si Mn Ph S Southern_Bentonite

Table 9: SAS Linear Regression Output for Vertical Model Subset

Analysis of Variance					
Source	DF	Sum of Squares	Mean Square	F Value	Pr > F
Model	7	0.01334	0.00191	4.76	0.0016
Error	25	0.01001	0.00040037		
Corrected Total	32	0.02335			

Root MSE	0.02001	R-Square	0.5713
Dependent Mean	0.06936	Adj R-Sq	0.4513
Coeff Var	28.84690		

Parameter Estimates						
Variable	DF	Parameter Estimate	Standard Error	t Value	Pr > |t|	Variance Inflation
Intercept	1	0.24222	0.07148	3.39	0.0023	0
Side	1	0.00734	0.00703	1.04	0.3064	1.01709
Pouring_Rate	1	0.00839	0.00276	3.04	0.0054	1.26251
Si	1	-0.09636	0.02881	-3.34	0.0026	3.51215
Mn	1	0.10332	0.02701	3.83	0.0008	1.69190
Ph	1	-1.90946	0.43334	-4.41	0.0002	2.53724
S	1	0.18596	0.14451	1.29	0.2099	4.14866
Southern_Bentonite	1	-0.00144	0.00052621	-2.74	0.0113	4.11079

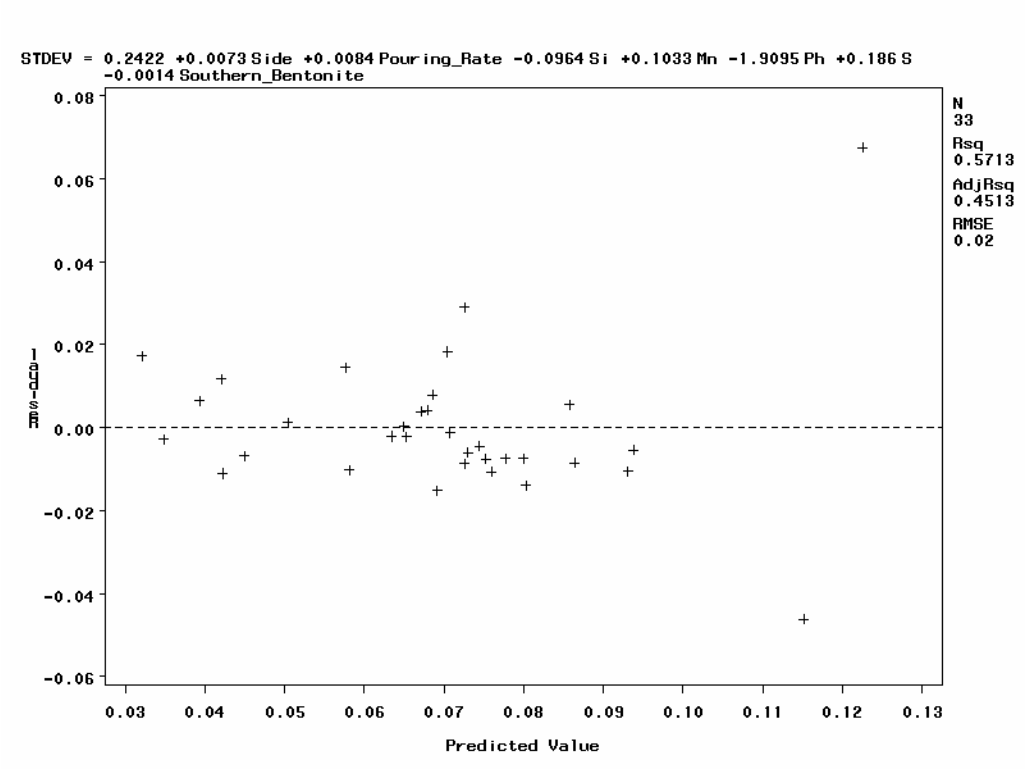

Figure 39: Residuals for Vertical Model Subset

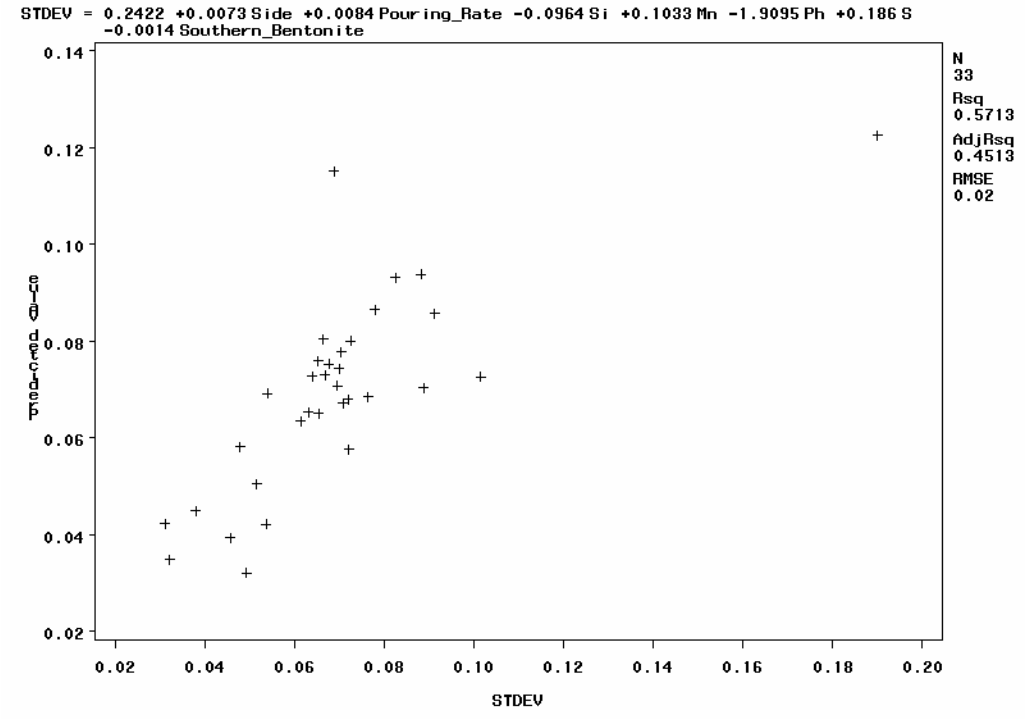

Figure 40: Regression for Standard Deviation (mm), Vertical Model Subset

The regression for the horizontally parted pattern data again required a subset selection (not shown). The best potential subset contained 7 parameters and the regression is shown in Table 10 and Figure 42 through Figure 44.

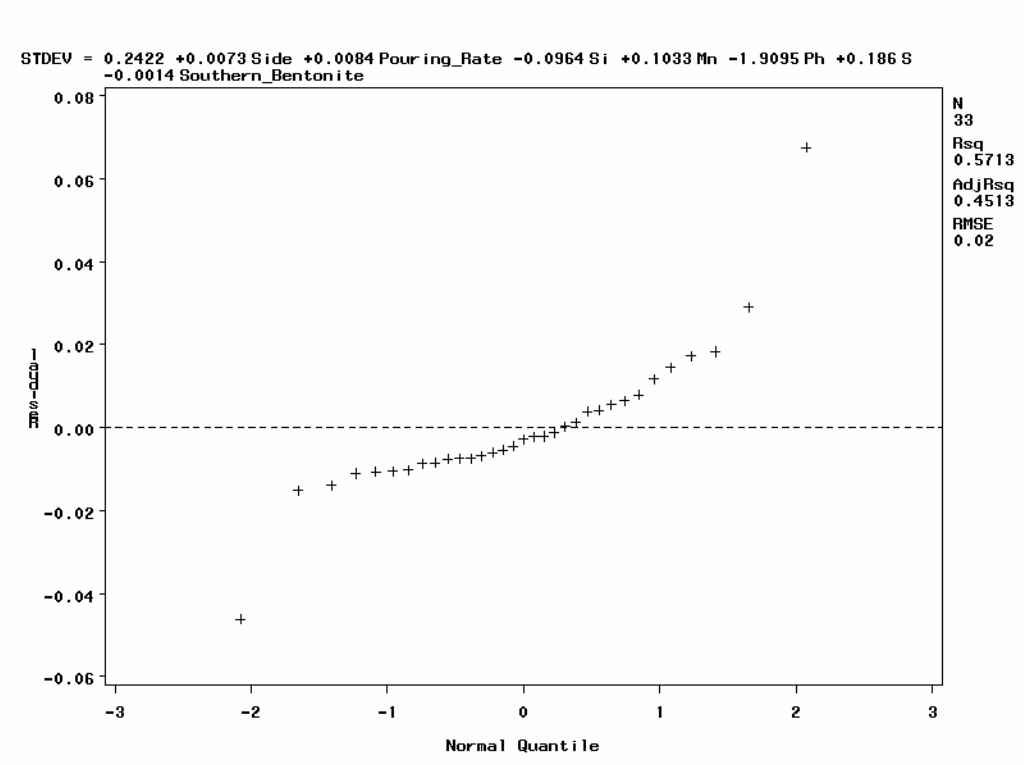

Figure 41: Normal Probability Plot, Vertical Model Subset

Table 10: SAS Linear Regression Output for Horizontal Model Subset

Subset: Ra Pouring_Rate Mn S Cu Western_Bentonite Permeability

Analysis of Variance					
Source	DF	Sum of Squares	Mean Square	F Value	Pr > F
Model	7	0.64853	0.09265	11.16	<.0001
Error	45	0.37342	0.00830		
Corrected Total	52	1.02195			

Root MSE	0.09109	R-Square	0.6346
Dependent Mean	0.33607	Adj R-Sq	0.5778
Coeff Var	27.10573		

Parameter Estimates						
Variable	DF	Parameter Estimate	Standard Error	t Value	Pr > |t|	Variance Inflation
Intercept	1	-0.14963	0.16310	-0.92	0.3638	0
Ra	1	0.05499	0.01648	3.34	0.0017	1.36235
Pouring_Rate	1	-0.02524	0.01124	-2.25	0.0297	3.16585
Mn	1	0.53433	0.20253	2.64	0.0114	4.00155
S	1	-3.21343	0.72868	-4.41	<.0001	5.08659
Cu	1	-0.45801	0.14038	-3.26	0.0021	3.09471
Western_Bentonite	1	0.00298	0.00078962	3.78	0.0005	1.92954
Permeability	1	0.00172	0.00081103	2.12	0.0392	2.72352

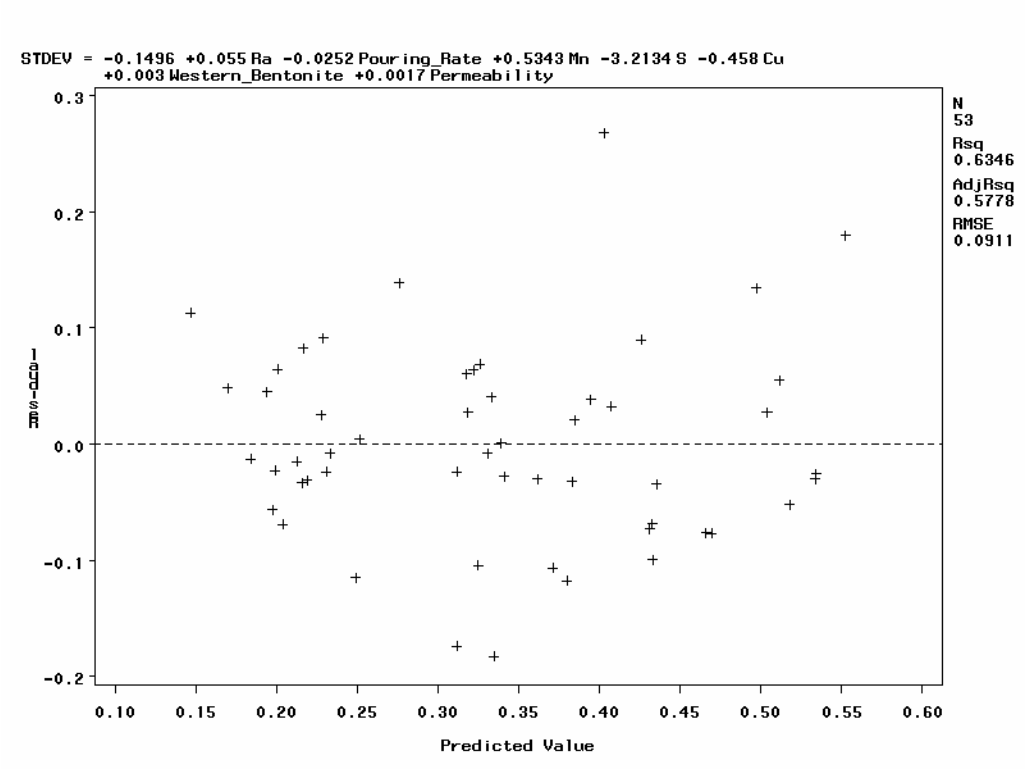

Figure 42: Residuals for Horizontal Model Subset

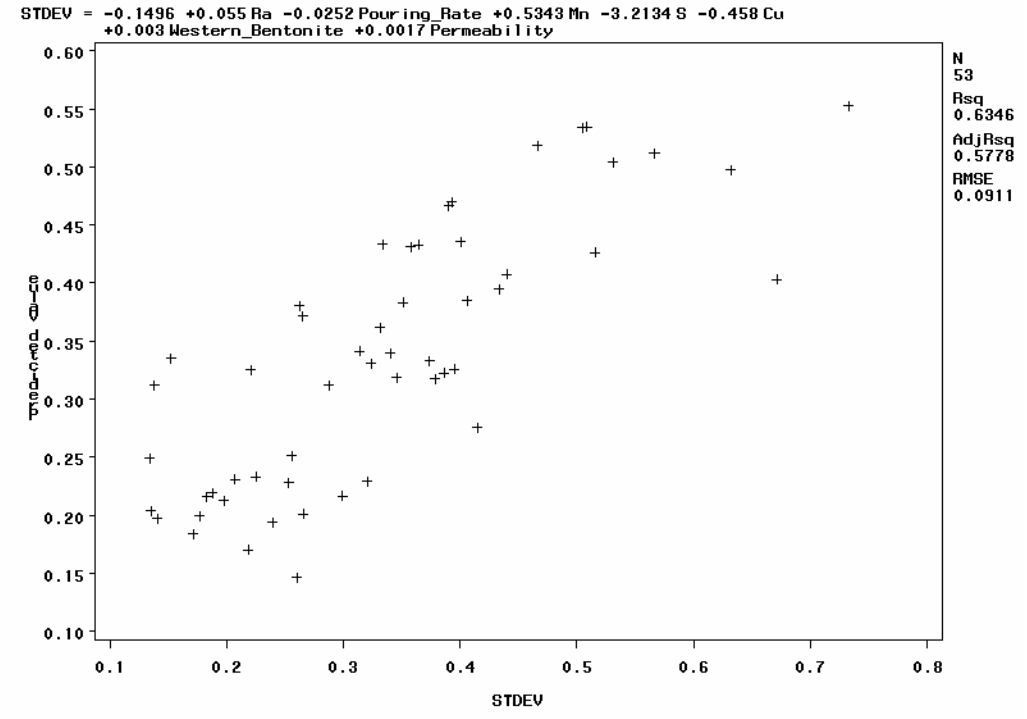

Figure 43: Regression for Standard Deviation (mm), Horizontal Model Subset

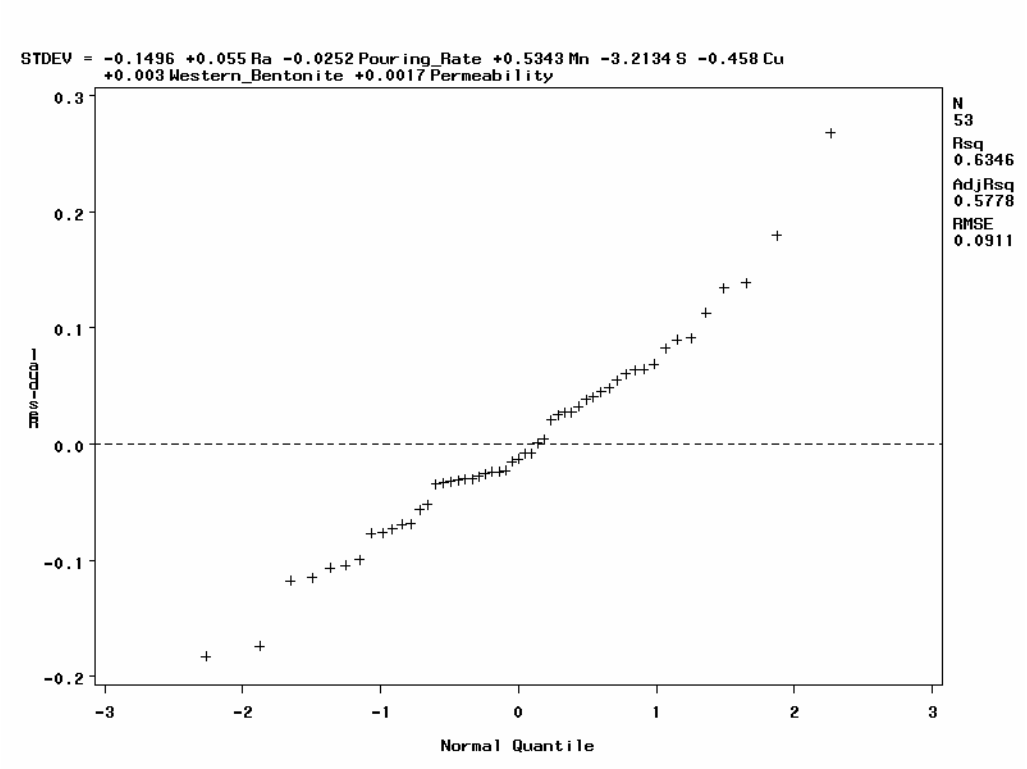

Figure 44: Normal Probability Plot, Horizontal Model Subset

The "horizontal" regression subset yielded an R^2 value of 0.6346. Additionally, the P-values were all relatively low except for pouring rate (with a value of 0.0297) and permeability (with a value of 0.0392). There were no serious problems with linearity when considering the residuals and the regression plots and in comparison to the vertical pattern regression the normal probability plot shows the regression to be relatively normal.

Comparison of Horizontal and Vertical Models to Full Model

Each of the fits was compared to determine the most efficient method for treating the data. To do this, the significant parameters for each analysis were first identified, and then compared to the other analyses.

Table 11 and Table 12 show a table of the influences of each parameter for the full model subsets. From both of the Full Model Subsets we see that percent copper in the melt, the pattern type, and iron type are very significant. We can also infer the relationship of the parameters to standard deviation, i.e. they increase or decrease standard deviation by the sign of their coefficient. It should also be noted that both models are very closely related, with Compactability and percent Phosphorous the only differences.

Table 11: Evaluation of Regression Equation, Full Model, Subset 1

Parameter	Coefficient	Direction	P-Value	Relative Significance
Ra	0.03433	Increasing	0.0022	*Somewhat Sign.*
Side	-0.01990	Decreasing	0.2789	Less Significant
Pattern_Type	0.22793	Increasing	<.0001	***Very Significant***
Iron_Type	-0.10923	Decreasing	0.0003	***Very Significant***
Pouring_Temp	-0.00075453	Decreasing	0.1014	Less Significant
Pouring_Rate	-0.02396	Decreasing	0.0015	Somewhat Sign.
Mn	0.12257	Increasing	0.1289	Less Significant
Ph	-0.24983	Decreasing	0.4011	Less Significant
Cu	-0.40527	Decreasing	<.0001	***Very Significant***
Western_Bentonite	0.00184	Increasing	0.0056	Somewhat Sign.
Permeability	0.00130	Increasing	0.0341	Somewhat Sign.

Table 12: Evaluation of Regression Equation, Full Model, Subset 2

Parameter	Coefficient	Direction	P-Value	Relative Significance
Ra	0.03409	Increasing	0.0027	Less Significant
Side	-0.02047	Decreasing	0.2662	Less Significant
Pattern_Type	0.21913	Increasing	<.0001	***Very Significant***
Iron_Type	-0.11514	Decreasing	<.0001	***Very Significant***
Pouring_Temp	-0.00079755	Decreasing	0.0776	Less Significant
Pouring_Rate	-0.02320	Decreasing	0.0028	Less Significant
Mn	0.11494	Increasing	0.1667	Less Significant
Cu	-0.41095	Decreasing	<.0001	***Very Significant***
Western_Bentonite	0.00179	Increasing	0.0117	Less Significant
Permeability	0.00135	Increasing	0.0244	Less Significant
Compactability	-0.00165	Decreasing	0.4428	Less Significant

We also need to consider the individual fits for vertical and horizontal data. Although the R^2 values are somewhat lower, we know from the first model subsets and the shape of the regression functions (see Figure 34 and Figure 37, for the regression curves of the subsets to the full model) that pattern type is a factor and the individual parametric influences on either may differ from the full model. Table 13 and Table 14 summarize the parametric relationships for each of the pattern types.

Table 13: Evaluation of Regression Equation, Vertical Model Subset

Parameter	Coefficient	Direction	P-Value	Relative Significance
Side	0.00734	Increasing	0.3064	Less Significant
Pouring_Rate	0.00839	Increasing	0.0054	Somewhat Significant
Si	-0.09636	Decreasing	0.0026	Somewhat Significant
Mn	0.10332	Increasing	0.0008	**Very Significant**
Ph	-1.90946	Decreasing	0.0002	**Very Significant**
S	0.18596	Increasing	0.2099	Less Significant
Southern_Bentonite	-0.00144	Decreasing	0.0113	Less Significant

The vertical pattern model shows a tendency for more influence from the metal constituents than do the full models and a dependency on Southern Bentonite content. Other sand/clay factors do not appear.

Table 14: Evaluation of Regression Equation, Horizontal Model Subset

Parameter	Coefficient	Direction	P-Value	Relative Significance
Ra	0.05499	Increasing	0.0017	Somewhat Significant
Pouring_Rate	-0.02524	Decreasing	0.0297	Less Significant
Mn	0.53433	Increasing	0.0114	Less Significant
S	-3.21343	Decreasing	<.0001	**Very Significant**
Cu	-0.45801	Increasing	0.0021	Somewhat Significant
Western_Bentonite	0.00298	Increasing	0.0005	**Very Significant**
Permeability	0.00172	Increasing	0.0392	Less Significant

The horizontal regression indicates more similarities to the full model than does the vertical regression. Here Ra, pouring rate, Manganese and Copper content in the melt, Western Bentonite percentage, and mold permeability are all parameters that appear in the full model regressions (Note however that the percent copper seems to influence standard deviation positively in the horizontal regression and does the opposite in the full model).

Metrology Round Robin

The role of coordinate measuring machines in foundries has historically been somewhat different than in other industries. In the foundry layout room, the CMM is often used simply to see if there is enough material at specific gage points – measurement techniques such as establishing complex datum reference frames and considering the number and spacing of sample points are usually not an issue. However, as modern foundries develop better production techniques to make competitive thin wall and precision castings, the measuring methods must keep pace. The goal of this study was to examine the measurement techniques used by various metrology shops, and assess the best measurement practices to reduce the variations in measurements. A set of 10 castings were sent to different metrology shops, and the measurement techniques and thickness results were recorded for each shop. The thickness of the castings reported by each metrology shop is compared to other shops in a method similar to a Gage Repeatability and Reproducibility (GR&R) study. We discuss the data obtained from these measurements, and then propose a procedure to reduce the variation caused due to different measurement techniques.

Objective of Metrology Round Robin

The objective of this work was to quantify the effects of different Coordinate Measuring Machine (CMM) strategies used by different measuring facilities (both industrial and laboratory) in inspecting cast iron parts. This is important for our thin-wall parts because the manufacturing process cannot be controlled more accurately than the capability of the measuring methods.

The basic premise in the metrology round robin is that the dimensional data obtained from different facilities should agree. If this is not the case, we will attempt to determine the root cause of these differences. The initial concerns we had about the round robin were in conveying the location of the measurement points and how the measurement values were reported. To help alleviate this problem, participants were given a detailed picture showing the orientation of the part and the coordinate system they should use to report the locations of the measured points. This picture is shown below in Figure 45.

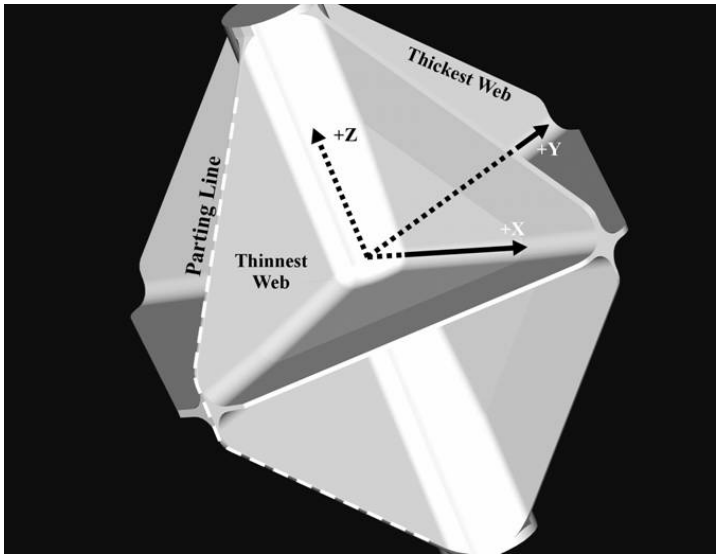

Figure 45: Coordinate system suggestion.

We had originally asked each participant to measure the thickness of the triangular webs at several points on each web, and report these thicknesses along with the straightness of the web edge and the flatness of the web surface. There was a lot of confusion among the participants about the straightness and flatness reporting, and

the data obtained for these values was not very reliable. For our analysis we focus on the measurement of three thickness values for each web, where the measurements are taken approximately 15mm from the edge of the web.

What we found – through discussions with the participants – was that the picture provided was incomplete, and additional information was needed to obtain a repeatable coordinate system. Of interest was the fact that different CMM operators requested very different information, and processed it in different ways. For example, simply holding the parts was addressed differently as shown in Figure 46. The fixture at left shows the central cylinder of the part (z-axis) held in the horizontal direction, while the fixture on the right holds the cylinder vertically. Theoretically, this will have no influence on the part measurements as the parts do not deform due to gravitational forces. However, the part may be held more firmly in one fixture, and the order in which the part features are measured may have an impact on the final results.

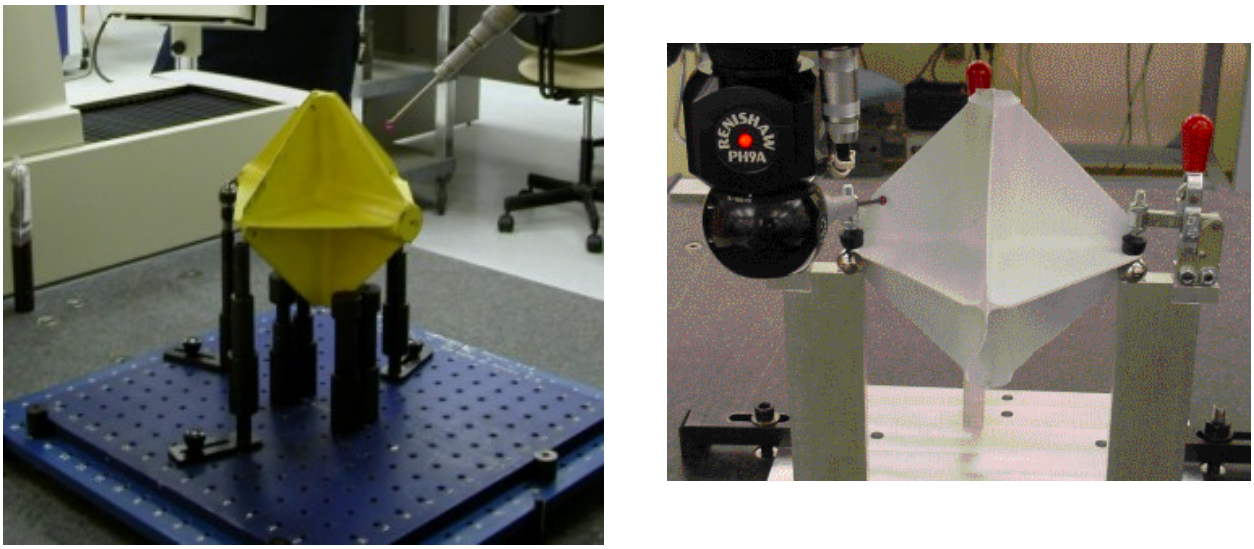

Figure 46: Different fixturing methods used by different participants.

Procedure for Metrology Round Robin

There were five participants in the initial measurement study (a sixth participant has just completed the measurements, which will be included in a final summary). All of the CMMs were bridge type machines; two were in well-controlled metrology labs, one was in an office environment, and two were in layout rooms at foundries. As discussed above, each participant was instructed to set up a reference coordinate system corresponding to the picture in Figure 45. They were then to measure 3 thicknesses on each of the 12 webs. A thickness measurement consisted of taking one point on each side of the web, nominally opposite one another. The midpoint of each pair of points was reported, as well as the distance between the two points. These thickness measurements were taken 15mm from the edge of each web, where the draft angle was minimal, in an attempt to limit the uncertainty due to the non-parallel nature of the cast surfaces.

We point out here that point measurement on these castings is not a trivial task when using a CMM. The measurements obtained from a CMM are based on the center of the stylus ball, and must be corrected for the radius of the ball. If we are measuring a regular geometric feature (such as a circle), we can first calculate the circle from the stylus center data, and then correct for the size of the stylus. When individual points are

measured, we don't know the surface direction in which to correct, or if the stylus made contact with a surface irregularity when the point was measured. For this reason, we expected to see some variation between the participants' results.

Results of Metrology Round Robin

We found that the ranges of values reported for the parts was much larger than anticipated. Whether this was due to fixturing methods, the method in which the coordinate system was established, or environmental differences is not completely clear at this time. Table 15 below shows the variation (in terms of standard deviation) of the different webs for each of the measurement participants. The web data are sorted from highest standard deviation to lowest. The standard deviation represents the deviation seen across all ten parts, and represents the combination of the part variation and the measurement variation due to the measuring equipment and procedures.

Table 15: Data from round-robin (A-E denote different participants).

	Standard Deviation in thickness					
WEB	A	B	C	D	E	Average
10	1.01056	0.185578	0.040308372	0.191101767	0.015299814	0.28857
3	0.136702	0.107096	0.135729002	0.72170557	0.126491432	0.245545
11	0.753583	0.074239	0.117969181	0.152250221	0.093535085	0.238315
9	0.801515	0.067572	0.101239343	0.028699515	0.062700816	0.212346
12	0.741611	0.050017	0.072805254	0.037164836	0.037735277	0.187867
4	0.412391	0.045997	0.049312281	0.232409573	0.036704667	0.155363
1	0.266364	0.141546	0.168705325	0.034832866	0.098907845	0.142071
2	0.196911	0.043023	0.081093353	0.039571842	0.04954406	0.082029
8	0.052777	0.075521	0.051324235	0.113619313	0.031525275	0.064953
6	0.044672	0.041363	0.058575406	0.13144823	0.040620456	0.063336
5	0.049519	0.05695	0.066157292	0.028978946	0.036989975	0.047719
7	0.059462	0.046317	0.062779788	0.036565145	0.022204707	0.045466

Let x_{nwip} be the thickness of the nth point (of the 3 points measured) on the wth web for the ith part (of 10) at the pth participant (of 5). The value in Table 15 for Web 10, Participant A (for example) is equal to

$$\underset{i=1\ldots10}{Std\ Dev}\left(\bar{x}_{wip}\right),$$ where $\bar{x}_{wip}$ is the average of the three points on web 10 (w=10) for participant A (p=A).

Figure 47 shows the variation in the web thickness for our 10 parts, ordered from largest to smallest. It is interesting to note that the four parting line webs (1, 3, 9, and 11) all have fairly large deviations from part to part. These parts are from a vertical parting line (DISA) machine, and this may be due to variations in pressure causing mold separation changes.

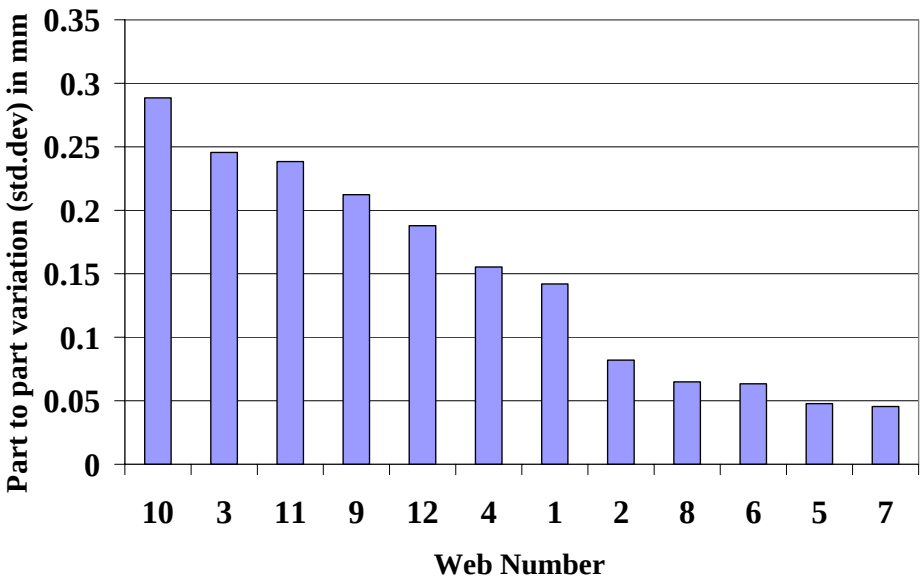

Figure 47: The difference in thickness between the parts –known as part-to-part variation in Gage R&R studies.

Figure 48 shows the deviations between different participants in their thickness measurements. This shows how – on average – the measurements from one CMM differed from the other participants. The different participants are indicated by color, so the maroon bars all correspond to the same measuring machine. The magnitude of these differences is surprising: The average of all 10 part measurements (30 points total) on web number 6 were **over 1.2 mm different** for the "blue" and "white" participants. While we expected to see some deviations, this was larger than anticipated.

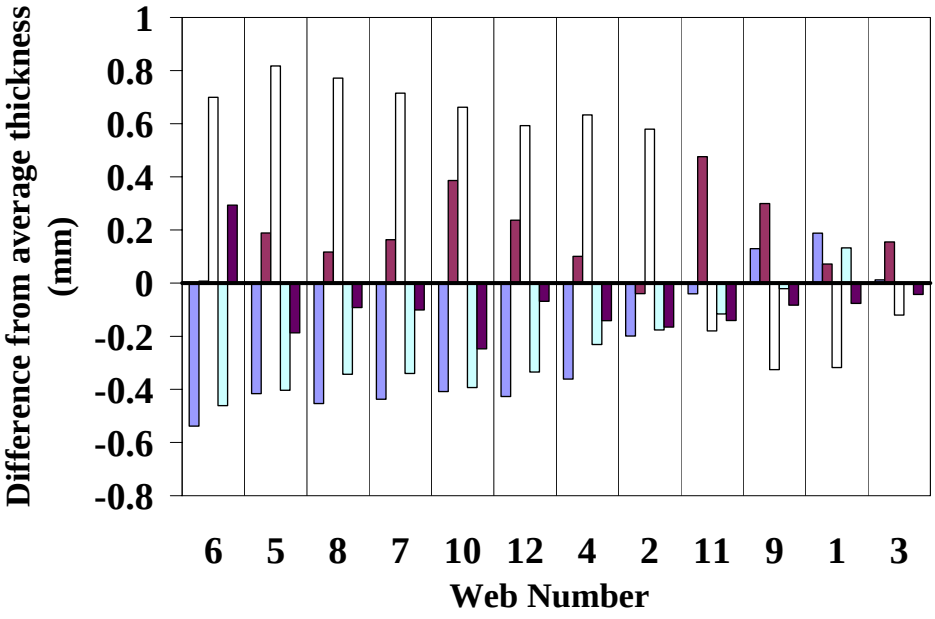

Figure 48: Deviations from the average thickness values, by participant.

Further work

At this time we believe that the two major contributors to the differences in the participants measurements are the uncertainty in the specification of the coordinate system (relying on the picture) and the basic qualification or calibration of the CMM probes (large bias in some of the results). To study this, additional tests with datum targets specified as per ASME Standard Y14.8M *Castings and Forgings* should be performed. In addition, it will also be useful to have the participants measure a machined artifact as well as the castings to assess the ability of their CMM to correctly measure a low-uncertainty artifact.

Surface Roughness / Waviness Study

Initial results from the research made it clear how important it is to separate the "bulk" dimensional size of the components from the surface effects. The surface wavelength composition study of thin wall iron castings was conducted using castings obtained from both the horizontal and vertical castings discussed earlier.

The outline of the full surface finish study is shown in Figure 50. Data were collected from the surface of a sample casting using both a surface profilometer and a CMM. A variety of analyses are performed to establish how the data obtained from these different methods can be correlated, and how this information relates to the bulk geometry of the cast part. The various steps involved in the surface finish study are discussed in this section and the combination and comparison of the different data are explained in the following section.

STEP 1: CMM MEASUREMENTS

When using discrete point measurement mode, CMM programmers must plan programs so that the tradeoff between the amount of time required to collect points on the surface (often more than 1 second per point) is balanced by the number of points sufficient to adequately characterize the surface. In industrial settings, the cost of the time required to measure a part often has higher priority, and thus a dozen or fewer points is a common measurement strategy for a surface the size of the web that we measure in this study. "Scanning CMMs" are able to collect data while scanning the surface with continual contact between the probe and part, but the influence of surface roughness and scanning speed on the accuracy of the measured data is not well understood. In this view of measurement, taking over one hundred discrete points in a line across the part can certainly be viewed as a high density scan. High density CMM measurements were taken approximately at the center on one of the webs – (web 3), which is the thinnest undrafted web – using a 6 mm diameter probe tip on a Brown & Sharpe CMM using PCDMIS software. The "cut web" (it was physically cut from the casting) and the path used for both the CMM and profile measurements are shown in Figure 49. The overall length of the cut web is 110 mm and the height from the top vertex to the bottom of the web along the measurement path as shown in Figure 49 is 57 mm. For the CMM measurements, both sides (top and bottom) of the web was measured without reorienting the part by rotating the probe with a Renishaw PH10 articulating probe head. Thickness values were calculated and reported at each point. Data analysis is explained in the next section.

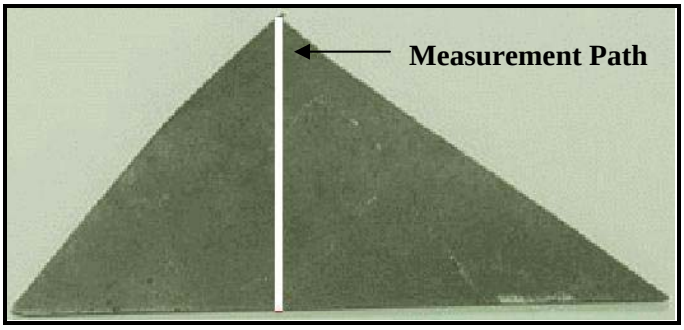

Figure 49: Cut web showing the path for CMM and Surface Measurements

STEP2: SURFACE MEASUREMENTS

The surface measurements were taken using a Somicronic Surfascan 3CS profilometer in approximately the same location on the cut web as the CMM measurements, on both top and bottom of the web. These points have a 0.008 μm spacing and 30 mm evaluation length.

STEP 3:

Point thickness values were calculated from the CMM measurements as shown in Figure 51.

STEP 4:

Non-filtered 2D surface profiles of both top and bottom of the web were obtained from the surface measurements as shown in Figure 52(a).

STEP 5:

The surface data was filtered and the roughness and waviness profiles were obtained for both the top and bottom of the web, as shown in Figure 52(b) and Figure 52(c).

STEP 6:

A least squares line was fit through the CMM data and it was interpolated to match the same number of data points as the surface measurements (3750 points) so that they could be added with the surface profiles and thickness calculations could be performed from them.

STEP 7:

The CMM least squares line was added to each of the profiles of the surface data (raw profile, roughness profile, waviness profile) of the top and bottom of the web respectively as shown in Figure 53(a),Figure 53(b), and Figure 53(c).

STEP 8:

The data points from Figure 53(a), Figure 53(b), and Figure 53(c) are averaged to obtain a total of 20 points for top and bottom of the web. This made the data more manageable while maintaining the characteristics of the surface.

STEP 9:

The CMM point thickness values were averaged to obtain the same number of points as the averaged surface profiles, as shown in Figure 54.

STEP 10:

Point thickness values are computed from the averaged wavelength profile points by adding the absolute values of the top and bottom profiles (raw profiles, roughness profile and waviness profile) respectively as shown in Figure 55.

STEP 11:

The surface data obtained from the profilometer were filtered using a morphological filter for both the top and bottom of the web. The morphological filtered surface data was averaged to obtain a total of 20 points to match the same number of points as the averaged CMM and surface profile points.

STEP 12:

Thickness values were calculated from the averaged morphological filtered data as shown in Figure 56.

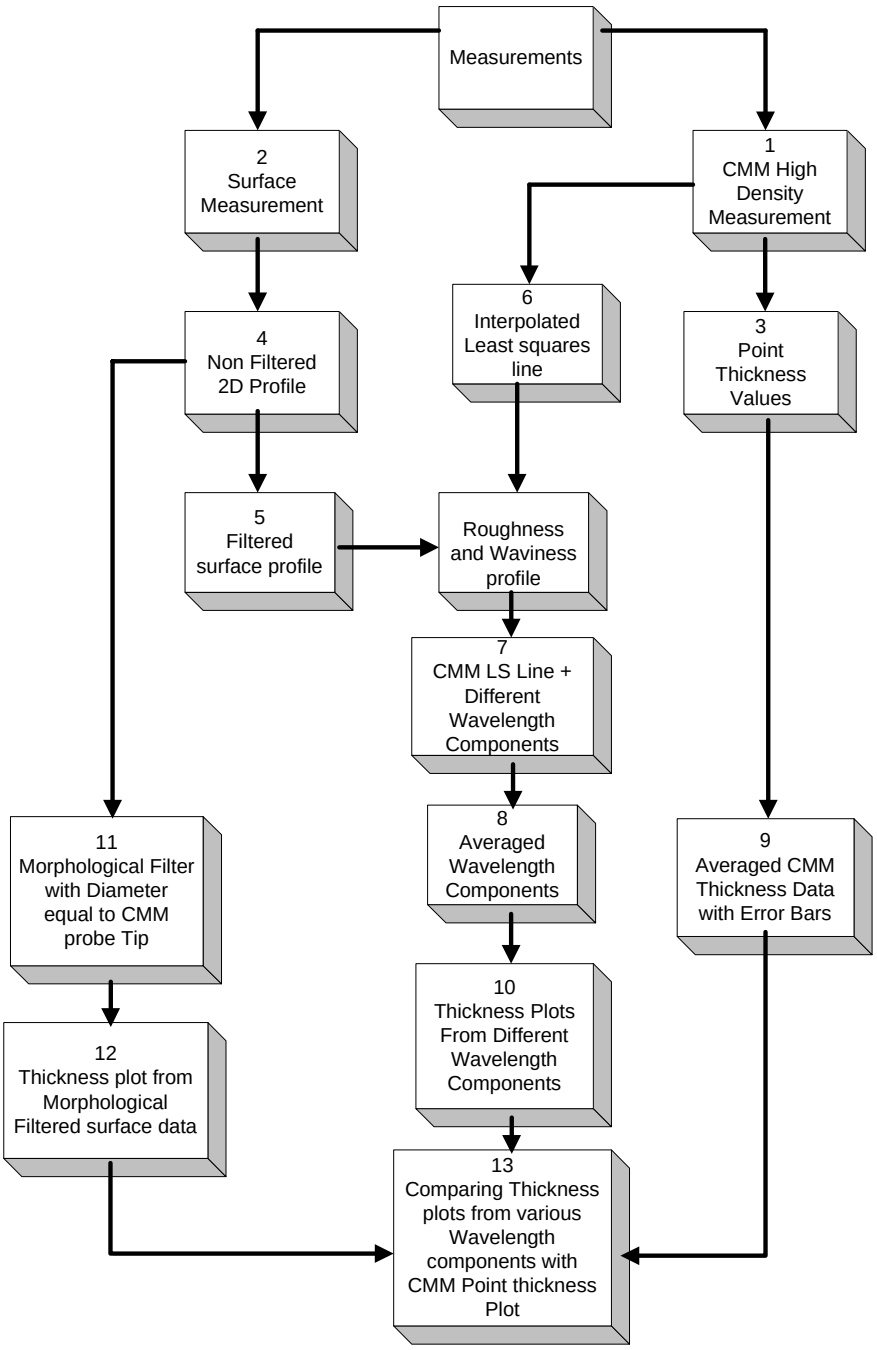

Figure 50: Surface finish study outline.

Data Analysis and Results

The initial measurements were taken using the CMM. A dense series of probings was taken on the top surface, and then a matching series of points on the other side of the web was taken. The measurement length or the sampling interval for the CMM data is approximately 50 mm. The point thickness values are calculated based on the location of the probe center when contact was registered with the part. Each point measured on the surface must compensate for the effective probe radius, as the CMM only tracks the unique center point of the probe. The data obtained from the CMM are shown in Figure 51. Several initial observations can be made from these data. The first is that there is a definite structure to the thickness data that is well within the CMM's capability for discernment (CMM repeatability < 4 μm and scale resolution = 0.5 μm, compared with hundreds

of µm of variability shown in the figure). It can be seen from this figure that there is variation in the web thickness as the points were measured across the face of the web.

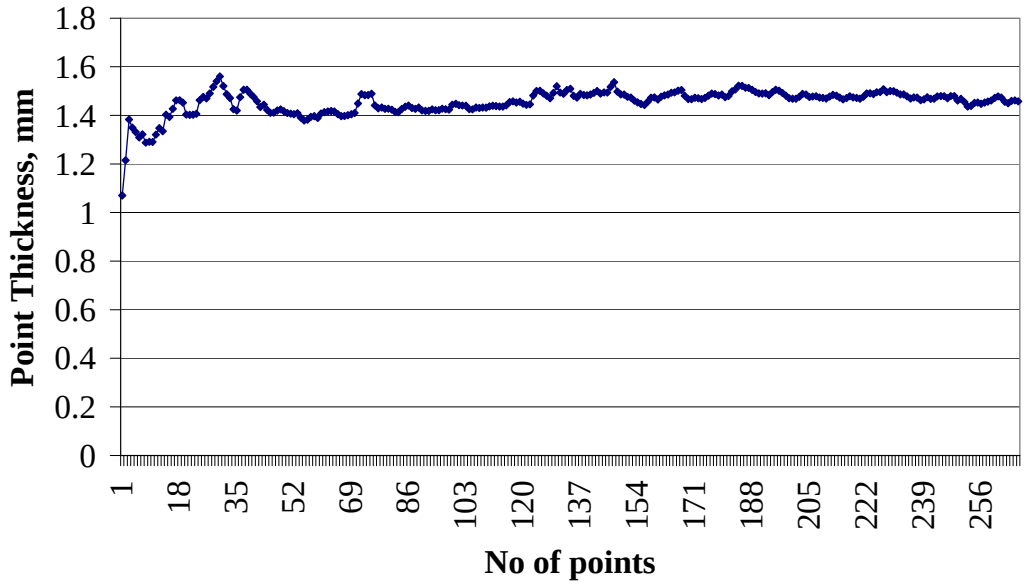

Figure 51: CMM point-to-point thickness data

The standard procedure for analyzing surface texture is to take a slow continuous scan across the part surface with a very small diameter stylus. The filtering of the data is done by software embedded in the instrument, although the user can select the spatial wavelength at which the data are separated into "Roughness" and "Waviness." For our study, the surface data were filtered using a standard Gaussian filter with 0.8 m as the cut-off frequency between roughness and waviness. The raw profile, the roughness profile, and waviness profile from the filtered surface data is shown in Figure 52(a), Figure 52(b), and Figure 52(c), correspondingly.

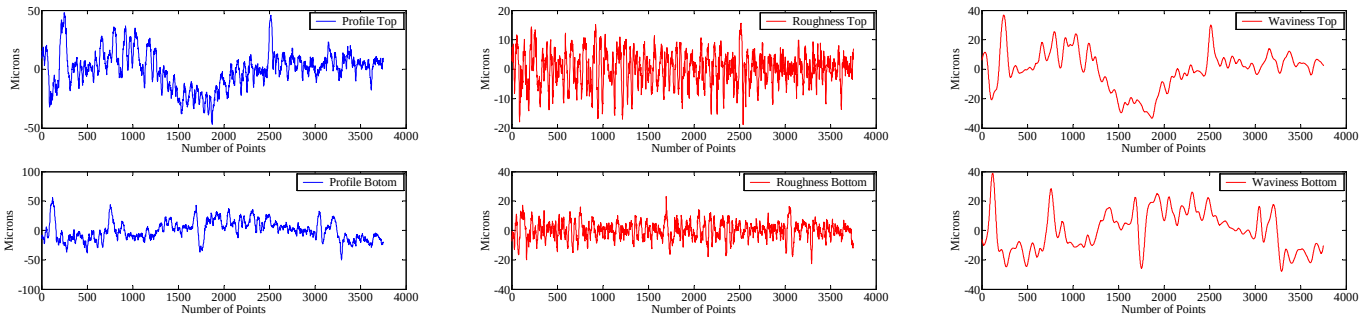

(a) full profile (b) roughness components (c) waviness components

Figure 52: Top and bottom profiles of the sample, and the filtered wavelength components.

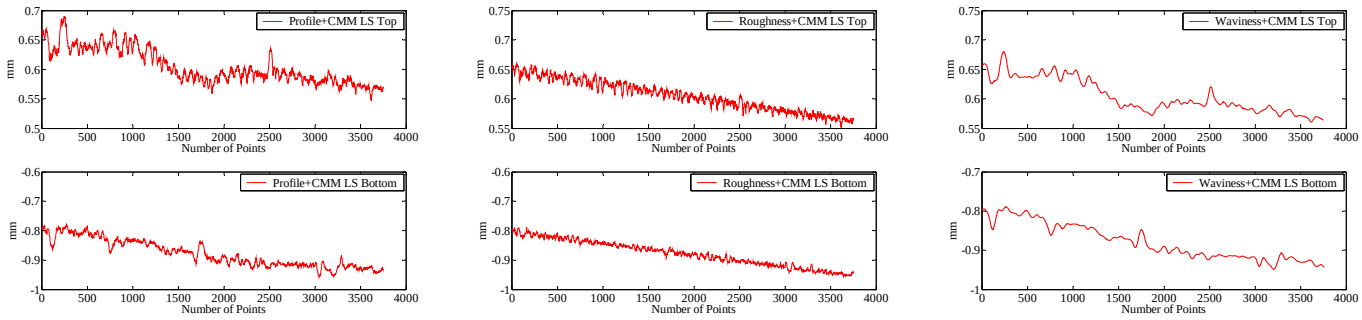

(a) LS line + full profile (b) LS line + roughness components (c) LS line + waviness components

Figure 53: CMM fitted line with superimposed components.

Two least-squares lines were fit through the CMM top and bottom data points, respectively. This creates ideal surfaces upon which profiles of roughness and waviness from the profilometer could be added and evaluated in comparison to the CMM points. This is shown in Figure 53(a), Figure 53(b), and Figure 53(c), where the raw profile, the roughness profile, and the waviness profile were each added to the CMM least squares line. Common CMM practice is to simply use the fitted line – called the substitute geometry – to represent the actual part surface, and distances are calculated from these substitute geometries. This is a reasonable choice for dealing with prismatic, machined parts, but unreliable for the sort of surfaces we have on cast iron parts.
The high density CMM measurements contained a total of 269 data points. To quantify the uncertainty present at the measurement points, 20 sets of points were used. These points were determined by averaging points together in groups of 10 (the first several points were removed from the sample). This averaging helped reduce the influence of sharp changes in the surface of the part, while retaining enough data to both show the character of the surface and estimate the variability from point to point on the surface.

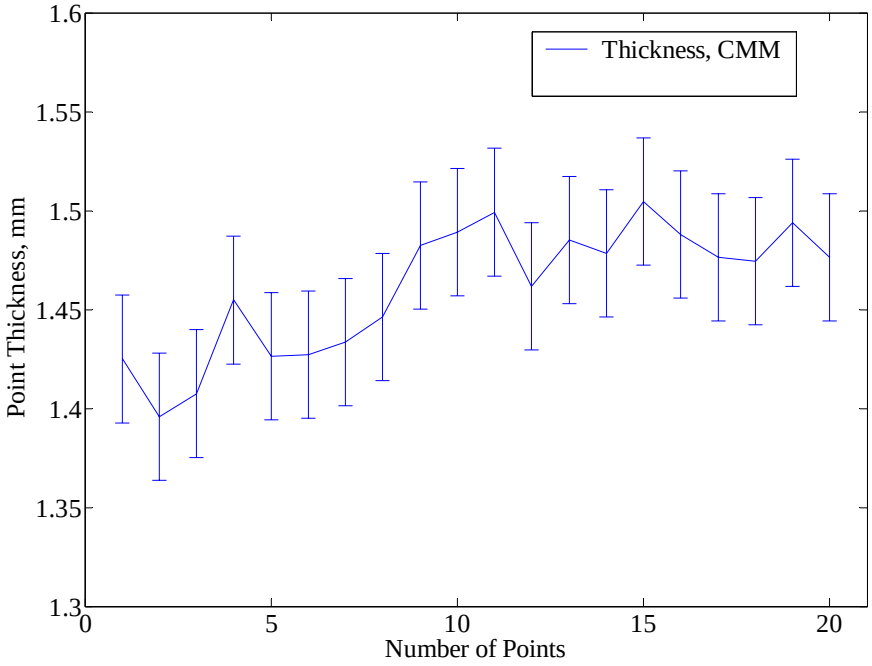

Figure 54: Averaged CMM thickness data with error bars.

The result of the averaging described above is shown in Figure 54, with error bars indicating one standard deviation of the group of ten measurement points. Using a similar technique, 20 points were extracted from the profile, roughness, and waviness curves in Figure 53 to create the plots in Figure 55(a),Figure 55 (b) and Figure 55(c). These plots are created by comparing the absolute values of the top and bottom profiles and adding them to make the comparisons to the CMM data possible.

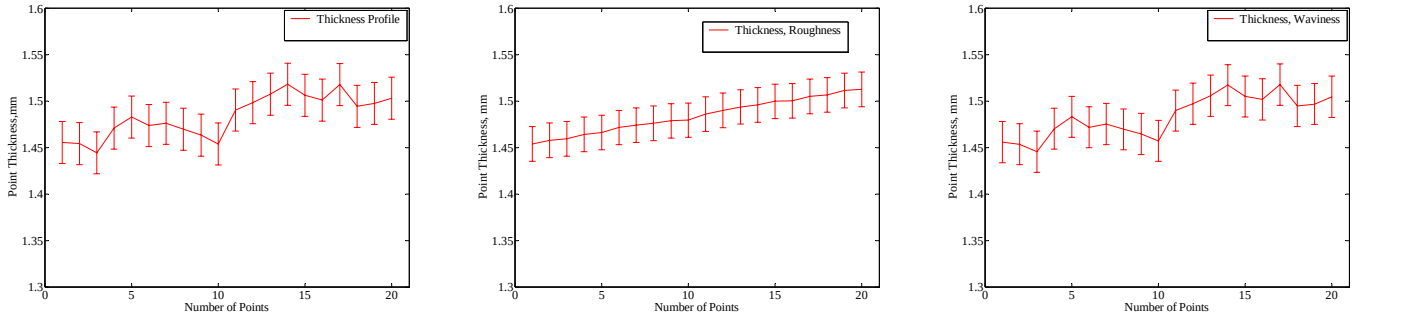

(a) LS line + full profile (b) LS line + roughness components (c) LS line + waviness components

Figure 55: Thickness from surface data.

Finally, the surface data in Figure 53(a) (the raw profile plus the CMM least squares fit) were filtered using a morphological filter. The morphological filter simulates a ball equal to the CMM probe tip diameter used – in this case, 6 mm. The same procedure as described above for the surface data was adapted to reduce the number of points and obtain the thickness values. These values, with their one sigma error bars, are shown in Figure 56. We then compared the various thickness plots to study the effects of the different wavelength components on the variation in actual thickness of the parts.

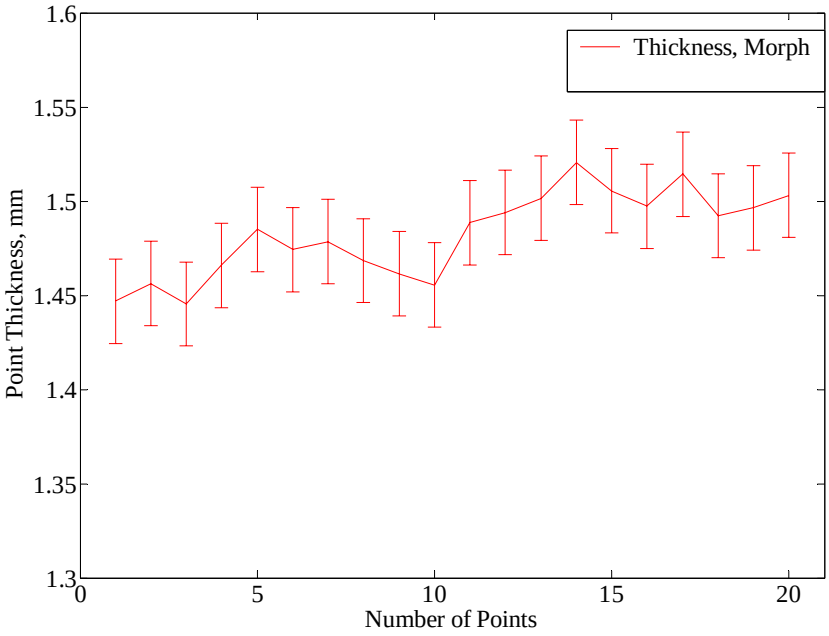

Figure 56: Thickness From Morphological Filtered Data

The data points from Figure 54, Figure 55, and Figure 56 were used to compute the average thickness, range of the thickness and standard deviation in thickness values as shown in Table 16. By comparing the standard deviation in thickness, the roughness profile had the least value followed by waviness profile and the full profile. The standard deviations from the morphological filtered data, waviness profile and the full profile varied on the nanometer level from one another. The variation obtained from the roughness profile is much less than that of the variation obtained from the waviness profile. Also, the variation obtained from the morphological filter is comparably equal to the variation obtained from the CMM data thus showing that the various filtering techniques correctly portray the effects of the filtering of the CMM stylus.

Table 16: Analysis of the various thickness data

Thickness From the corresponding Data	Average Thickness (mm)	Range of Thickness (mm)	Standard Deviation in Thickness (mm)
CMM	1.4612	0.1087	0.0321
Full Profile	1.4838	0.0739	0.0226
Roughness profile	1.4840	0.0585	0.0185
Waviness profile	1.4837	0.0721	0.0221
Morphological Filtered data	1.4825	0.0751	0.0223

Conclusion

Regression analyses were used to determine the influence of the various pouring parameters on dimensional variation. The regressions indicated that an empirical relationship could be determined with an R^2 value of 0.79, indicating a relatively strong relationship given the complexity of the foundry process. It was also clear that significant differences existed between horizontal and vertical molding machines in terms of the resulting dimensional variation. However, when the two machines were analyzed separately, R^2 values dropped due to the reduced number of data.

The indications are therefore that while the full model subsets are more statistically sound, there is room for an improved modeling, most likely one that considers interactions, particularly with the pattern type variable. Considering the vertical and horizontal models, although less likely to be an accurate fit, could allow some offset or modification of the full model to find the best fit for the specific end result desired. Namely, to decrease variation in thin cast iron features one could use the full model(s) and apply changes to the parameters based on the specific pattern (vertical or horizontal) to be used and the corresponding pattern model (vertical or horizontal).

A significant difference in variations obtained from vertical vs. horizontal molding machines was also noticed. When analyzed separately, however, the resulting empirical relationships for horizontal and vertical machines had reduced R^2 values, probably due to the reduced data sets. Significant parameters affecting variability included surface roughness, pattern type, iron type, pouring rate, copper content, amount of Western Bentonite, permeability, Manganese, Sulfer, Silicon, and Phosophorus content in the melt.

The metrology round robin results were startling, showing excessive differences from one foundry to another in reporting dimensions. Results from this portion of the study were severe, indicating a strong need for metrology training and standardization in the industry.

Finally, it was determined that the surface waviness had more impact on dimensional variation than does surface roughness. The exception to this rule is when burn-in occurs, which is very detrimental to dimensional repeatability. Burn-in occurred much more frequently in the horizontal castings, partly because of the lower clay content, higher temperatures, and lower compactability.

It is believed that the knowledge learned in this study, if applied, will lead to dimensionally improved castings. The empirical relationships yield insights into the parameters that most negatively affect dimensional repeatability, and also provide a tool for predicting the tradeoffs of using various parameters.

Budget

The final budget for the project is shown in Table 17. Total expenditures charged to the Department of Energy were 14% under budget. 50% cost share was realized despite the loss of a significant sponsor who had committed $40,000 in-kind / year but who closed its doors during the depressed economy. Total expense to the DOE was $371,295. Total project expenditures including industry cost share was $755,063.

Table 17: Approved Budget

			Approved Spending Plan			Actual Spent to Date		
Phase / Budget Period			DOE Amount	Cost Share	Total	DOE Amount	Cost Share	Total
	From	To						
Year 1	1-Jan-02	31-Dec-02	$188,739	$205,750	$394,489	$144,444	$70,857	$215,301
Year 2	1-Jan-03	31-Dec-03	$213,644	$205,750	$419,394	$160,056	$183,059	$343,115
Year 3	1-Jan-03	15-July-03	No-cost extension			$66,795	$129,852	$196,647
		Totals	**$432,383**	**$441,500**	**$873,883**	**$371,295**	**$383,768**	**$755,063**

Appendix

Table 18: R-Square Subset Selection for Full Model

Number in Model	R-Square	C(p)	Variables in Model
1	0.4710	68.6599	Pattern_Type
1	0.3431	100.9896	Ra
1	0.2928	113.7019	Permeability
1	0.2441	125.9997	Mg
1	0.2168	132.8820	Iron_Type
2	0.6054	36.7014	Pattern_Type MBClay
2	0.5891	40.8196	Pattern_Type Ph
2	0.5888	40.8885	Pattern_Type Compactability
2	0.5734	44.7829	Pattern_Type Iron_Type
2	0.5527	50.0156	Pattern_Type S
3	0.6504	27.3316	Ra Iron_Type Western_Bentonite
3	0.6484	27.8479	Ra S Western_Bentonite
3	0.6461	28.4161	Pattern_Type C MBClay
3	0.6450	28.6912	Ra Iron_Type Moisture
3	0.6441	28.9380	Pouring_Rate Western_Bentonite Permeability
4	0.7241	10.7133	Ra Pattern_Type S Western_Bentonite
4	0.7233	10.9137	Ra Pattern_Type Iron_Type Western_Bentonite
4	0.7184	12.1637	Ra S Western_Bentonite Permeability
4	0.7174	12.4080	Ra Pattern_Type Iron_Type Cu
4	0.7027	16.1142	Ra Iron_Type Western_Bentonite Green_Comp
5	0.7460	7.1818	Ra Iron_Type Western_Bentonite GFN Permeability
5	0.7437	7.7657	Ra Pattern_Type Iron_Type Cu Western_Bentonite
5	0.7436	7.7852	Ra S Western_Bentonite GFN Permeability
5	0.7434	7.8295	Ra Iron_Type Western_Bentonite Southern_Bentonite Permeability
5	0.7431	7.9001	Ra Pattern_Type Iron_Type Cu GFN
6	0.7631	4.8517	Ra Pattern_Type Iron_Type Cu GFN Compactability
6	0.7625	5.0137	Ra Pattern_Type Iron_Type S Cu GFN
6	0.7597	5.7170	Ra Pattern_Type Iron_Type Cu Western_Bentonite Southern_Bentonite
6	0.7587	5.9811	Ra Iron_Type Cu Western_Bentonite GFN Permeability
6	0.7583	6.0665	Ra Iron_Type Cu Western_Bentonite Southern_Bentonite Permeability
7	0.7759	3.6116	Ra Pattern_Type Iron_Type S Cu GFN Permeability
7	0.7745	3.9886	Ra Pattern_Type Iron_Type Cu Western_Bentonite GFN Permeability
7	0.7735	4.2325	Ra Pattern_Type Iron_Type Cu Southern_Bentonite GFN Permeability
7	0.7734	4.2538	Ra Pattern_Type Iron_Type Cu GFN Permeability Compactability
7	0.7726	4.4593	Ra Pattern_Type Iron_Type Si S Cu GFN
8	0.7827	3.9104	Ra Side Pattern_Type Iron_Type S Cu GFN Permeability
8	0.7825	3.9652	Ra Pattern_Type Iron_Type Pouring_Rate S Cu GFN Permeability

8	0.7812	4.2915	Ra Side Pattern_Type Iron_Type Cu Western_Bentonite GFN Permeability
8	0.7804	4.4786	Ra Side Pattern_Type Iron_Type Cu GFN Permeability Compactability
8	0.7804	4.4980	Ra Pattern_Type Iron_Type S Cu GFN Permeability Compactability
9	0.7899	4.0897	Ra Pattern_Type Iron_Type Pouring_Rate S Mg Cu GFN Permeability
9	0.7893	4.2324	Ra Side Pattern_Type Iron_Type Pouring_Rate S Cu GFN Permeability
9	0.7871	4.7857	Ra Side Pattern_Type Iron_Type S Cu GFN Permeability Compactability
9	0.7865	4.9387	Ra Pattern_Type Iron_Type Si S Mg Cu GFN MBClay
9	0.7865	4.9542	Ra Side Pattern_Type Iron_Type Si S Cu GFN Permeability
10	0.7968	4.3359	Ra Side Pattern_Type Iron_Type Pouring_Rate S Mg Cu GFN Permeability
10	0.7928	5.3532	Ra Side Pattern_Type Iron_Type Si S Mg Cu GFN MBClay
10	0.7923	5.4802	Ra Pattern_Type Iron_Type Pouring_Rate S Mg Cu GFN Permeability Green_Comp
10	0.7922	5.5178	Ra Pattern_Type Iron_Type Pouring_Rate Si S Mg Cu GFN Permeability
10	0.7920	5.5467	Ra Side Pattern_Type Iron_Type Pouring_Rate S Cu Western_Bentonite GFN Permeability
11	0.7992	5.7282	Ra Side Pattern_Type Iron_Type Pouring_Rate S Mg Cu GFN Permeability Green_Comp
11	0.7991	5.7720	Ra Side Pattern_Type Iron_Type Pouring_Rate Si S Mg Cu GFN Permeability
11	0.7980	6.0276	Ra Side Pattern_Type Iron_Type Pouring_Rate S Mg Cu Southern_Bentonite GFN Permeability
11	0.7979	6.0718	Ra Side Pattern_Type Iron_Type Pouring_Rate S Mg Cu Western_Bentonite GFN Permeability
11	0.7978	6.0780	Ra Side Pattern_Type Iron_Type Pouring_Rate S Mg Cu GFN Permeability Compactability
12	0.8031	6.7576	Ra Side Pattern_Type Iron_Type Pouring_Rate Si S Mg Cu GFN Permeability Green_Comp
12	0.8012	7.2301	Ra Side Pattern_Type Iron_Type Pouring_Rate Si S Mg Cu GFN Permeability MBClay
12	0.8003	7.4498	Ra Side Pattern_Type Iron_Type Pouring_Temp Pouring_Rate Si S Mg Cu GFN Permeability
12	0.8002	7.4951	Ra Side Pattern_Type Iron_Type Pouring_Rate C Si S Mg Cu GFN Permeability
12	0.8002	7.4965	Ra Side Pattern_Type Iron_Type Pouring_Rate Si S Mg Cu Southern_Bentonite GFN Permeability
13	0.8048	8.3311	Ra Side Pattern_Type Iron_Type Pouring_Rate C Si S Mg Cu GFN Permeability Green_Comp
13	0.8042	8.4853	Ra Side Pattern_Type Iron_Type Pouring_Rate Si Mn S Mg Cu GFN Permeability Green_Comp
13	0.8034	8.6665	Ra Side Pattern_Type Iron_Type Pouring_Rate Si S Mg Cu Southern_Bentonite GFN Permeability Green_Comp
13	0.8034	8.6735	Ra Side Pattern_Type Iron_Type Pouring_Rate Si S Mg Cu GFN Permeability Green_Comp MBClay
13	0.8033	8.6975	Ra Side Pattern_Type Iron_Type Pouring_Temp

			Pouring_Rate Si S Mg Cu GFN Permeability Green_Comp
14	0.8067	9.8330	Ra Side Pattern_Type Iron_Type Pouring_Rate C Si Mn S Mg Cu GFN Permeability Green_Comp
14	0.8049	10.2882	Ra Side Pattern_Type Iron_Type Pouring_Rate C Si S Mg Cu GFN Permeability Compactability Green_Comp
14	0.8049	10.2970	Ra Side Pattern_Type Iron_Type Pouring_Temp Pouring_Rate C Si S Mg Cu GFN Permeability Green_Comp
14	0.8049	10.2972	Ra Side Pattern_Type Iron_Type Pouring_Rate C Si S Mg Cu GFN Moisture Permeability Green_Comp
14	0.8049	10.2998	Ra Side Pattern_Type Iron_Type Pouring_Rate C Si S Mg Cu Southern_Bentonite GFN Permeability Green_Comp
15	0.8070	11.7729	Ra Side Pattern_Type Iron_Type Pouring_Rate C Si Mn S Mg Cu GFN Permeability Compactability Green_Comp
15	0.8069	11.7812	Ra Side Pattern_Type Iron_Type Pouring_Rate C Si Mn S Mg Cu Southern_Bentonite GFN Permeability Green_Comp
15	0.8068	11.8156	Ra Side Pattern_Type Iron_Type Pouring_Rate C Si Mn S Mg Cu GFN Permeability Green_Comp MBClay
15	0.8068	11.8225	Ra Side Pattern_Type Iron_Type Pouring_Rate C Si Mn S Mg Cu Western_Bentonite GFN Permeability Green_Comp
15	0.8068	11.8242	Ra Side Pattern_Type Iron_Type Pouring_Rate C Si Mn Ph S Mg Cu GFN Permeability Green_Comp
16	0.8075	13.6275	Ra Side Pattern_Type Iron_Type Pouring_Rate C Si Mn S Mg Cu Western_Bentonite Southern_Bentonite GFN Permeability Green_Comp
16	0.8074	13.6570	Ra Side Pattern_Type Iron_Type Pouring_Rate C Si Mn Ph S Mg Cu GFN Permeability Compactability Green_Comp
16	0.8074	13.6752	Ra Side Pattern_Type Iron_Type Pouring_Rate C Si Mn S Mg Cu Southern_Bentonite GFN Permeability Compactability Green_Comp
16	0.8071	13.7299	Ra Side Pattern_Type Iron_Type Pouring_Rate C Si Mn S Mg Cu Western_Bentonite GFN Permeability Compactability Green_Comp
16	0.8071	13.7464	Ra Side Pattern_Type Iron_Type Pouring_Rate C Si Mn S Mg Cu GFN Permeability Compactability Green_Comp MBClay
17	0.8080	15.5157	Ra Side Pattern_Type Iron_Type Pouring_Temp Pouring_Rate C Si Mn S Mg Cu Western_Bentonite Southern_Bentonite GFN Permeability Green_Comp
17	0.8078	15.5736	Ra Side Pattern_Type Iron_Type Pouring_Rate C Si Mn S Mg Cu Western_Bentonite Southern_Bentonite GFN Moisture Permeability Green_Comp
17	0.8077	15.5828	Ra Side Pattern_Type Iron_Type Pouring_Rate C Si Mn S Mg Cu Western_Bentonite Southern_Bentonite GFN Permeability Compactability Green_Comp
17	0.8077	15.5978	Ra Side Pattern_Type Iron_Type Pouring_Rate C Si Mn Ph S Mg Cu Western_Bentonite Southern_Bentonite GFN Permeability Green_Comp
17	0.8076	15.6028	Ra Side Pattern_Type Iron_Type Pouring_Temp Pouring_Rate C Si Mn S Mg Cu Southern_Bentonite GFN Permeability Compactability Green_Comp
18	0.8084	17.4123	Ra Side Pattern_Type Iron_Type Pouring_Temp Pouring_Rate C Si Mn S Mg Cu Western_Bentonite

			Southern_Bentonite GFN Permeability Compactability Green_Comp
18	0.8083	17.4389	Ra Side Pattern_Type Iron_Type Pouring_Rate C Si Mn S Mg Cu Western_Bentonite Southern_Bentonite GFN Moisture Permeability Compactability Green_Comp
18	0.8082	17.4571	Ra Side Pattern_Type Iron_Type Pouring_Rate C Si Mn Ph S Mg Cu Western_Bentonite Southern_Bentonite GFN Permeability Compactability Green_Comp
18	0.8081	17.4756	Ra Side Pattern_Type Iron_Type Pouring_Temp Pouring_Rate C Si Mn S Mg Cu Western_Bentonite Southern_Bentonite GFN Moisture Permeability Green_Comp
18	0.8081	17.4760	Ra Side Pattern_Type Iron_Type Pouring_Temp Pouring_Rate C Si Mn Ph S Mg Cu Western_Bentonite Southern_Bentonite GFN Permeability Green_Comp
19	0.8095	19.1253	Ra Side Pattern_Type Iron_Type Pouring_Rate C Si Mn Ph S Mg Cu Western_Bentonite Southern_Bentonite GFN Moisture Permeability Compactability Green_Comp
19	0.8094	19.1571	Ra Side Pattern_Type Iron_Type Pouring_Temp Pouring_Rate C Si Mn Ph S Mg Cu Western_Bentonite Southern_Bentonite GFN Permeability Compactability Green_Comp
19	0.8091	19.2234	Ra Side Pattern_Type Iron_Type Pouring_Rate Si Mn Ph S Mg Cu Western_Bentonite Southern_Bentonite GFN Moisture Permeability Compactability Green_Comp MBClay
19	0.8090	19.2531	Ra Side Pattern_Type Iron_Type Pouring_Temp Pouring_Rate C Si Mn S Mg Cu Western_Bentonite Southern_Bentonite GFN Moisture Permeability Compactability Green_Comp
19	0.8085	19.3788	Ra Side Pattern_Type Iron_Type Pouring_Rate C Si Mn S Mg Cu Western_Bentonite Southern_Bentonite GFN Moisture Permeability Compactability Green_Comp MBClay
20	0.8127	20.3349	Ra Side Pattern_Type Iron_Type Pouring_Temp Pouring_Rate Si Mn Ph S Mg Cu Western_Bentonite Southern_Bentonite GFN Moisture Permeability Compactability Green_Comp MBClay
20	0.8113	20.6695	Ra Side Pattern_Type Iron_Type Pouring_Temp Pouring_Rate C Si Mn Ph S Mg Cu Western_Bentonite Southern_Bentonite GFN Moisture Permeability Compactability Green_Comp
20	0.8105	20.8900	Ra Side Pattern_Type Iron_Type Pouring_Rate C Si Mn Ph S Mg Cu Western_Bentonite Southern_Bentonite GFN Moisture Permeability Compactability Green_Comp MBClay
20	0.8095	21.1347	Ra Side Pattern_Type Iron_Type Pouring_Temp Pouring_Rate C Si Mn S Mg Cu Western_Bentonite Southern_Bentonite GFN Moisture Permeability Compactability Green_Comp MBClay
20	0.8094	21.1569	Ra Side Pattern_Type Iron_Type Pouring_Temp Pouring_Rate C Si Mn Ph S Mg Cu Western_Bentonite Southern_Bentonite GFN Permeability Compactability Green_Comp MBClay

Table 19: R-Square Subset Selection for Modified Full Model

Number in Model	R-Square	C(p)	Variables in Model
1	0.5685	63.4792	Pattern_Type
1	0.4025	117.9123	Permeability
1	0.3527	134.2471	Ra
1	0.1769	191.8870	Mg
1	0.1506	200.5038	Si
2	0.6630	34.5155	Pattern_Type Ph
2	0.6551	37.0912	Pattern_Type Compactability
2	0.6326	44.4649	Pattern_Type Iron_Type
2	0.6197	48.6930	Pattern_Type S
2	0.6139	50.6058	Pattern_Type Mg
3	0.6866	28.7524	Ra Pattern_Type Ph
3	0.6833	29.8345	Pattern_Type Ph Cu
3	0.6812	30.5337	Pattern_Type C Ph
3	0.6810	30.6073	Ra Pattern_Type Compactability
3	0.6790	31.2621	Ra Pattern_Type Iron_Type
4	0.7262	17.7674	Pattern_Type Pouring_Rate Ph Cu
4	0.7191	20.1143	Pattern_Type S Cu Compactability
4	0.7190	20.1349	Ra Pattern_Type Iron_Type Cu
4	0.7173	20.6965	Pattern_Type Iron_Type Cu Compactability
4	0.7160	21.1286	Pattern_Type Ph S Cu
5	0.7491	12.2755	Pattern_Type Iron_Type Pouring_Rate Ph Cu
5	0.7469	12.9928	Ra Pattern_Type Iron_Type Pouring_Rate Cu
5	0.7452	13.5495	Ra Pattern_Type S Cu Compactability
5	0.7445	13.7608	Ra Pattern_Type Iron_Type Cu Compactability
5	0.7430	14.2628	Pattern_Type Iron_Type Pouring_Rate Cu Compactability
6	0.7686	7.8645	Ra Pattern_Type Iron_Type Pouring_Rate Ph Cu
6	0.7668	8.4523	Ra Pattern_Type Iron_Type Pouring_Rate Cu Compactability
6	0.7607	10.4573	Ra Pattern_Type Pouring_Rate Ph S Cu
6	0.7594	10.8969	Ra Pattern_Type Iron_Type Pouring_Rate Cu Western_Bentonite
6	0.7578	11.4179	Ra Pattern_Type Iron_Type Pouring_Rate Cu Southern_Bentonite
7	0.7829	5.1915	Ra Pattern_Type Iron_Type Pouring_Rate Ph Mg Cu
7	0.7740	8.1165	Ra Pattern_Type Iron_Type Pouring_Rate Ph Cu Western_Bentonite
7	0.7733	8.3324	Ra Pattern_Type Iron_Type Pouring_Rate Mg Cu Compactability
7	0.7727	8.5235	Ra Side Pattern_Type Iron_Type Pouring_Rate Ph Cu
7	0.7718	8.8149	Ra Pattern_Type Iron_Type Pouring_Rate Ph Cu Compactability
8	0.7868	5.9001	Ra Side Pattern_Type Iron_Type Pouring_Rate Ph Mg Cu
8	0.7867	5.9516	Ra Pattern_Type Iron_Type Pouring_Rate Ph S Mg Cu
8	0.7865	6.0063	Ra Pattern_Type Iron_Type Pouring_Rate Si Ph Mg Cu
8	0.7863	6.0702	Ra Pattern_Type Iron_Type Pouring_Rate Ph Mg Cu Permeability
8	0.7860	6.1780	Ra Pattern_Type Iron_Type Pouring_Rate Mn Ph Mg Cu

9	0.7921	6.1673	Ra Pattern_Type Iron_Type Pouring_Rate Si Mn Ph Mg Cu
9	0.7920	6.1984	Ra Pattern_Type Iron_Type Pouring_Rate Mn Ph Mg Cu Permeability
9	0.7912	6.4662	Ra Pattern_Type Iron_Type Pouring_Rate Ph S Mg Cu Permeability
9	0.7904	6.7173	Ra Side Pattern_Type Iron_Type Pouring_Rate Ph Mg Cu Permeability
9	0.7904	6.7344	Ra Side Pattern_Type Iron_Type Pouring_Rate Si Ph Mg Cu
10	0.7974	6.4232	Ra Pattern_Type Iron_Type Pouring_Rate Mn Ph Mg Cu Western_Bentonite Permeability
10	0.7960	6.8957	Ra Pattern_Type Iron_Type Pouring_Rate Mn Ph Mg Cu GFN Permeability
10	0.7959	6.9136	Ra Side Pattern_Type Iron_Type Pouring_Rate Mn Ph Mg Cu Permeability
10	0.7957	6.9889	Ra Side Pattern_Type Iron_Type Pouring_Rate Si Mn Ph Mg Cu
10	0.7956	7.0249	Ra Pattern_Type Iron_Type Pouring_Rate Mn Ph Mg Cu Moisture Permeability
11	0.8027	6.6921	Ra Pattern_Type Iron_Type Pouring_Temp Pouring_Rate Mn Ph Mg Cu Western_Bentonite Permeability
11	0.8011	7.2173	Ra Side Pattern_Type Iron_Type Pouring_Rate Mn Ph Mg Cu Western_Bentonite Permeability
11	0.8010	7.2631	Ra Pattern_Type Iron_Type Pouring_Temp Pouring_Rate Mn Ph Mg Cu Southern_Bentonite Permeability
11	0.8003	7.4816	Ra Side Pattern_Type Iron_Type Pouring_Rate Mn Ph Mg Cu GFN Permeability
11	0.8000	7.5705	Ra Pattern_Type Iron_Type Pouring_Rate Si Mn Ph Mg Cu GFN Permeability
12	0.8063	7.5167	Ra Side Pattern_Type Iron_Type Pouring_Temp Pouring_Rate Mn Ph Mg Cu Western_Bentonite Permeability
12	0.8046	8.0731	Ra Pattern_Type Iron_Type Pouring_Temp Pouring_Rate Si Mn Ph Mg Cu Western_Bentonite Permeability
12	0.8043	8.1811	Ra Pattern_Type Iron_Type Pouring_Temp Pouring_Rate Mn Ph S Mg Cu Western_Bentonite Permeability
12	0.8042	8.1902	Ra Side Pattern_Type Iron_Type Pouring_Temp Pouring_Rate Mn Ph Mg Cu Southern_Bentonite Permeability
12	0.8042	8.2042	Ra Side Pattern_Type Iron_Type Pouring_Rate Si Mn Ph Mg Cu GFN Permeability
13	0.8080	8.9460	Ra Side Pattern_Type Iron_Type Pouring_Temp Pouring_Rate Si Mn Ph Mg Cu Western_Bentonite Permeability
13	0.8077	9.0384	Ra Side Pattern_Type Iron_Type Pouring_Temp Pouring_Rate Mn Ph S Mg Cu Western_Bentonite Permeability
13	0.8064	9.4644	Ra Side Pattern_Type Iron_Type Pouring_Temp Pouring_Rate Mn Ph Mg Cu Western_Bentonite Moisture Permeability
13	0.8064	9.4836	Ra Side Pattern_Type Iron_Type Pouring_Temp Pouring_Rate Mn Ph Mg Cu Western_Bentonite Permeability Compactability
13	0.8063	9.5038	Ra Side Pattern_Type Iron_Type Pouring_Temp Pouring_Rate Mn Ph Mg Cu Western_Bentonite Southern_Bentonite Permeability
14	0.8088	10.6934	Ra Side Pattern_Type Iron_Type Pouring_Temp Pouring_Rate Si Mn Ph Mg Cu Southern_Bentonite GFN Permeability
14	0.8088	10.7081	Ra Side Pattern_Type Iron_Type Pouring_Temp Pouring_Rate Si Mn Ph S Mg Cu Western_Bentonite Permeability
14	0.8087	10.7302	Ra Side Pattern_Type Iron_Type Pouring_Temp Pouring_Rate Mn Ph S Mg Cu Southern_Bentonite GFN Permeability
14	0.8085	10.7925	Ra Side Pattern_Type Iron_Type Pouring_Temp Pouring_Rate Si Mn Ph Mg Cu Western_Bentonite Moisture Permeability
14	0.8084	10.8389	Ra Side Pattern_Type Iron_Type Pouring_Temp Pouring_Rate Si Mn Ph Mg Cu Western_Bentonite GFN Permeability
15	0.8102	12.2443	Ra Side Pattern_Type Iron_Type Pouring_Temp Pouring_Rate Si Mn Ph S Mg Cu Southern_Bentonite GFN Permeability
15	0.8093	12.5358	Ra Side Pattern_Type Iron_Type Pouring_Temp Pouring_Rate Si Mn Ph S Mg Cu

			Western_Bentonite GFN Permeability
15	0.8092	12.5494	Ra Side Pattern_Type Iron_Type Pouring_Temp Pouring_Rate Si Mn Ph S Mg Cu Western_Bentonite Moisture Permeability
15	0.8091	12.5992	Ra Side Pattern_Type Iron_Type Pouring_Temp Pouring_Rate Si Mn Ph Mg Cu Western_Bentonite GFN Moisture Permeability
15	0.8091	12.6013	Ra Side Pattern_Type Iron_Type Pouring_Temp Pouring_Rate Si Mn Ph Mg Cu Southern_Bentonite GFN Moisture Permeability
16	0.8107	14.0862	Ra Side Pattern_Type Iron_Type Pouring_Temp Pouring_Rate Si Mn Ph S Mg Cu Southern_Bentonite GFN Moisture Permeability
16	0.8106	14.1046	Ra Side Pattern_Type Iron_Type Pouring_Temp Pouring_Rate Si Mn Ph S Mg Cu Western_Bentonite Southern_Bentonite GFN Permeability
16	0.8103	14.1951	Ra Side Pattern_Type Iron_Type Pouring_Temp Pouring_Rate C Si Mn Ph S Mg Cu Southern_Bentonite GFN Permeability
16	0.8102	14.2226	Ra Side Pattern_Type Iron_Type Pouring_Temp Pouring_Rate Si Mn Ph S Mg Cu Southern_Bentonite GFN Permeability Compactability
16	0.8101	14.2626	Ra Side Pattern_Type Iron_Type Pouring_Temp Pouring_Rate Si Mn Ph S Mg Cu Western_Bentonite GFN Moisture Permeability
17	0.8108	16.0376	Ra Side Pattern_Type Iron_Type Pouring_Temp Pouring_Rate C Si Mn Ph S Mg Cu Southern_Bentonite GFN Moisture Permeability
17	0.8108	16.0475	Ra Side Pattern_Type Iron_Type Pouring_Temp Pouring_Rate C Si Mn Ph S Mg Cu Western_Bentonite Southern_Bentonite GFN Permeability
17	0.8107	16.0595	Ra Side Pattern_Type Iron_Type Pouring_Temp Pouring_Rate Si Mn Ph S Mg Cu Western_Bentonite Southern_Bentonite GFN Moisture Permeability
17	0.8107	16.0821	Ra Side Pattern_Type Iron_Type Pouring_Temp Pouring_Rate Si Mn Ph S Mg Cu Western_Bentonite Southern_Bentonite GFN Permeability Compactability
17	0.8107	16.0844	Ra Side Pattern_Type Iron_Type Pouring_Temp Pouring_Rate Si Mn Ph S Mg Cu Southern_Bentonite GFN Moisture Permeability Compactability
18	0.8109	18.0063	Ra Side Pattern_Type Iron_Type Pouring_Temp Pouring_Rate C Si Mn Ph S Mg Cu Western_Bentonite Southern_Bentonite GFN Moisture Permeability
18	0.8109	18.0126	Ra Side Pattern_Type Iron_Type Pouring_Temp Pouring_Rate C Si Mn Ph S Mg Cu Western_Bentonite Southern_Bentonite GFN Permeability Compactability
18	0.8108	18.0376	Ra Side Pattern_Type Iron_Type Pouring_Temp Pouring_Rate C Si Mn Ph S Mg Cu Southern_Bentonite GFN Moisture Permeability Compactability
18	0.8107	18.0587	Ra Side Pattern_Type Iron_Type Pouring_Temp Pouring_Rate Si Mn Ph S Mg Cu Western_Bentonite Southern_Bentonite GFN Moisture Permeability Compactability
18	0.8103	18.2064	Ra Side Pattern_Type Iron_Type Pouring_Temp Pouring_Rate C Si Mn Ph S Mg Cu Western_Bentonite GFN Moisture Permeability Compactability
19	0.8109	20.0000	Ra Side Pattern_Type Iron_Type Pouring_Temp Pouring_Rate C Si Mn Ph S Mg Cu Western_Bentonite Southern_Bentonite GFN Moisture Permeability Compactability

Table 20: R-Square Subset Selection for Remodified Full Model

Number in Model	R-Square	C(p)	Variables in Model
1	0.5685	55.5812	Pattern_Type
1	0.4025	106.9756	Permeability
1	0.3527	122.3985	Ra
1	0.1506	184.9565	Si
1	0.1386	188.6638	GFN
2	0.6630	28.3460	Pattern_Type Ph
2	0.6551	30.7780	Pattern_Type Compactability
2	0.6326	37.7400	Pattern_Type Iron_Type
2	0.6197	41.7321	Pattern_Type S
2	0.6135	43.6439	Ra Pattern_Type
3	0.6866	23.0163	Ra Pattern_Type Ph
3	0.6833	24.0380	Pattern_Type Ph Cu
3	0.6812	24.6982	Pattern_Type C Ph
3	0.6810	24.7677	Ra Pattern_Type Compactability
3	0.6790	25.3859	Ra Pattern_Type Iron_Type
4	0.7262	12.7562	Pattern_Type Pouring_Rate Ph Cu
4	0.7191	14.9720	Pattern_Type S Cu Compactability
4	0.7190	14.9915	Ra Pattern_Type Iron_Type Cu
4	0.7173	15.5217	Pattern_Type Iron_Type Cu Compactability
4	0.7160	15.9298	Pattern_Type Ph S Cu
5	0.7491	7.6825	Pattern_Type Iron_Type Pouring_Rate Ph Cu
5	0.7469	8.3597	Ra Pattern_Type Iron_Type Pouring_Rate Cu
5	0.7452	8.8854	Ra Pattern_Type S Cu Compactability
5	0.7445	9.0849	Ra Pattern_Type Iron_Type Cu Compactability
5	0.7430	9.5588	Pattern_Type Iron_Type Pouring_Rate Cu Compactability
6	0.7686	3.6294	Ra Pattern_Type Iron_Type Pouring_Rate Ph Cu
6	0.7668	4.1844	Ra Pattern_Type Iron_Type Pouring_Rate Cu Compactability
6	0.7607	6.0775	Ra Pattern_Type Pouring_Rate Ph S Cu
6	0.7594	6.4925	Ra Pattern_Type Iron_Type Pouring_Rate Cu Western_Bentonite
6	0.7578	6.9844	Ra Pattern_Type Iron_Type Pouring_Rate Cu Southern_Bentonite
7	0.7740	3.9789	Ra Pattern_Type Iron_Type Pouring_Rate Ph Cu Western_Bentonite
7	0.7727	4.3632	Ra Side Pattern_Type Iron_Type Pouring_Rate Ph Cu
7	0.7718	4.6384	Ra Pattern_Type Iron_Type Pouring_Rate Ph Cu Compactability
7	0.7717	4.6839	Ra Pattern_Type Iron_Type Pouring_Rate Ph Cu Southern_Bentonite
7	0.7715	4.7308	Ra Pattern_Type Iron_Type Pouring_Rate Ph Cu Moisture
8	0.7823	3.4057	Ra Pattern_Type Iron_Type Pouring_Temp Pouring_Rate Cu Southern_Bentonite Permeability
8	0.7796	4.2361	Ra Pattern_Type Iron_Type Pouring_Temp Pouring_Rate Cu Western_Bentonite Permeability
8	0.7784	4.5988	Ra Pattern_Type Iron_Type Pouring_Temp Pouring_Rate Ph Cu Southern_Bentonite
8	0.7784	4.6051	Ra Pattern_Type Iron_Type Pouring_Temp Pouring_Rate Ph Cu Western_Bentonite
8	0.7778	4.7943	Ra Pattern_Type Iron_Type Pouring_Rate Ph Cu Western_Bentonite Permeability

9	0.7882	3.5617	Ra Pattern_Type Iron_Type Pouring_Temp Pouring_Rate Mn Cu Western_Bentonite Permeability
9	0.7855	4.4054	Ra Side Pattern_Type Iron_Type Pouring_Temp Pouring_Rate Cu Southern_Bentonite Permeability
9	0.7852	4.5001	Ra Pattern_Type Iron_Type Pouring_Temp Pouring_Rate Cu Southern_Bentonite Permeability Compactability
9	0.7850	4.5615	Ra Pattern_Type Iron_Type Pouring_Temp Pouring_Rate Mn Cu Southern_Bentonite Permeability
9	0.7845	4.7212	Ra Pattern_Type Iron_Type Pouring_Temp Pouring_Rate S Cu Southern_Bentonite Permeability
10	0.7918	4.4443	Ra Side Pattern_Type Iron_Type Pouring_Temp Pouring_Rate Mn Cu Western_Bentonite Permeability
10	0.7913	4.6044	Ra Pattern_Type Iron_Type Pouring_Temp Pouring_Rate Mn Ph Cu Western_Bentonite Permeability
10	0.7901	4.9922	Ra Pattern_Type Iron_Type Pouring_Temp Pouring_Rate Mn Cu Western_Bentonite Permeability Compactability
10	0.7893	5.2381	Ra Pattern_Type Iron_Type Pouring_Temp Pouring_Rate Mn S Cu Western_Bentonite Permeability
10	0.7891	5.2999	Ra Pattern_Type Iron_Type Pouring_Temp Pouring_Rate Mn Cu Western_Bentonite Moisture Permeability
11	0.7949	5.5013	Ra Side Pattern_Type Iron_Type Pouring_Temp Pouring_Rate Mn Ph Cu Western_Bentonite Permeability
11	0.7939	5.8186	Ra Side Pattern_Type Iron_Type Pouring_Temp Pouring_Rate Mn Cu Western_Bentonite Permeability Compactability
11	0.7928	6.1471	Ra Side Pattern_Type Iron_Type Pouring_Temp Pouring_Rate Mn S Cu Western_Bentonite Permeability
11	0.7926	6.2239	Ra Side Pattern_Type Iron_Type Pouring_Temp Pouring_Rate Mn Cu Western_Bentonite Moisture Permeability
11	0.7923	6.2898	Ra Side Pattern_Type Iron_Type Pouring_Temp Pouring_Rate Cu Western_Bentonite Moisture Permeability Compactability
12	0.7955	7.3203	Ra Side Pattern_Type Iron_Type Pouring_Temp Pouring_Rate Si Mn Ph Cu Western_Bentonite Permeability
12	0.7952	7.3993	Ra Side Pattern_Type Iron_Type Pouring_Temp Pouring_Rate Mn Cu Western_Bentonite Moisture Permeability Compactability
12	0.7951	7.4246	Ra Side Pattern_Type Iron_Type Pouring_Temp Pouring_Rate Mn Ph Cu Western_Bentonite Permeability Compactability
12	0.7951	7.4437	Ra Side Pattern_Type Iron_Type Pouring_Temp Pouring_Rate Mn Ph S Cu Western_Bentonite Permeability
12	0.7950	7.4754	Ra Side Pattern_Type Iron_Type Pouring_Temp Pouring_Rate Mn Ph Cu Western_Bentonite Moisture Permeability
13	0.7957	9.2579	Ra Side Pattern_Type Iron_Type Pouring_Temp Pouring_Rate Si Mn Ph Cu Western_Bentonite Moisture Permeability
13	0.7956	9.2781	Ra Side Pattern_Type Iron_Type Pouring_Temp Pouring_Rate Si Mn Cu Western_Bentonite Moisture Permeability Compactability
13	0.7956	9.2819	Ra Side Pattern_Type Iron_Type Pouring_Temp Pouring_Rate Si Mn Ph Cu Western_Bentonite GFN Permeability
13	0.7956	9.2862	Ra Side Pattern_Type Iron_Type Pouring_Temp Pouring_Rate Si Mn Ph Cu Western_Bentonite Permeability Compactability
13	0.7955	9.2960	Ra Side Pattern_Type Iron_Type Pouring_Temp Pouring_Rate C Si Mn Ph Cu Western_Bentonite Permeability
14	0.7961	11.1319	Ra Side Pattern_Type Iron_Type Pouring_Temp Pouring_Rate Si Mn Ph Cu Western_Bentonite Moisture Permeability Compactability

14	0.7959	11.1874	Ra Side Pattern_Type Iron_Type Pouring_Temp Pouring_Rate Si Mn Ph Cu Western_Bentonite GFN Moisture Permeability
14	0.7959	11.1994	Ra Side Pattern_Type Iron_Type Pouring_Temp Pouring_Rate Si Mn Cu Western_Bentonite Southern_Bentonite Moisture Permeability Compactability
14	0.7959	11.2019	Ra Side Pattern_Type Iron_Type Pouring_Temp Pouring_Rate Si Mn Ph Cu Western_Bentonite Southern_Bentonite Moisture Permeability
14	0.7958	11.2237	Ra Side Pattern_Type Iron_Type Pouring_Temp Pouring_Rate C Si Mn Ph Cu Western_Bentonite Moisture Permeability
15	0.7964	13.0349	Ra Side Pattern_Type Iron_Type Pouring_Temp Pouring_Rate Si Mn Ph Cu Western_Bentonite Southern_Bentonite Moisture Permeability Compactability
15	0.7963	13.0547	Ra Side Pattern_Type Iron_Type Pouring_Temp Pouring_Rate Si Mn Ph Cu Western_Bentonite GFN Moisture Permeability Compactability
15	0.7963	13.0708	Ra Side Pattern_Type Iron_Type Pouring_Temp Pouring_Rate C Si Mn Ph Cu Western_Bentonite Moisture Permeability Compactability
15	0.7961	13.1278	Ra Side Pattern_Type Iron_Type Pouring_Temp Pouring_Rate Si Mn Ph S Cu Western_Bentonite Moisture Permeability Compactability
15	0.7960	13.1641	Ra Side Pattern_Type Iron_Type Pouring_Temp Pouring_Rate Si Mn Ph S Cu Western_Bentonite GFN Moisture Permeability
16	0.7965	15.0041	Ra Side Pattern_Type Iron_Type Pouring_Temp Pouring_Rate C Si Mn Ph Cu Western_Bentonite Southern_Bentonite Moisture Permeability Compactability
16	0.7964	15.0311	Ra Side Pattern_Type Iron_Type Pouring_Temp Pouring_Rate C Si Mn Ph Cu Western_Bentonite GFN Moisture Permeability Compactability
16	0.7964	15.0339	Ra Side Pattern_Type Iron_Type Pouring_Temp Pouring_Rate Si Mn Ph Cu Western_Bentonite Southern_Bentonite GFN Moisture Permeability Compactability
16	0.7964	15.0341	Ra Side Pattern_Type Iron_Type Pouring_Temp Pouring_Rate Si Mn Ph S Cu Western_Bentonite Southern_Bentonite Moisture Permeability Compactability
16	0.7964	15.0429	Ra Side Pattern_Type Iron_Type Pouring_Temp Pouring_Rate Si Mn Ph S Cu Western_Bentonite GFN Moisture Permeability Compactability
17	0.7965	17.0000	Ra Side Pattern_Type Iron_Type Pouring_Temp Pouring_Rate C Si Mn Ph S Cu Western_Bentonite Southern_Bentonite Moisture Permeability Compactability
17	0.7965	17.0034	Ra Side Pattern_Type Iron_Type Pouring_Temp Pouring_Rate C Si Mn Ph Cu Western_Bentonite Southern_Bentonite GFN Moisture Permeability Compactability
17	0.7965	17.0151	Ra Side Pattern_Type Iron_Type Pouring_Temp Pouring_Rate C Si Mn Ph S Cu Western_Bentonite GFN Moisture Permeability Compactability
17	0.7964	17.0316	Ra Side Pattern_Type Iron_Type Pouring_Temp Pouring_Rate Si Mn Ph S Cu Western_Bentonite Southern_Bentonite GFN Moisture Permeability Compactability
17	0.7961	17.1403	Ra Side Pattern_Type Iron_Type Pouring_Temp Pouring_Rate C Si Mn S Cu Western_Bentonite Southern_Bentonite GFN Moisture Permeability Compactability
18	0.7965	19.0000	Ra Side Pattern_Type Iron_Type Pouring_Temp Pouring_Rate C Si Mn Ph S Cu Western_Bentonite Southern_Bentonite GFN Moisture Permeability Compactability